A novel approach to localize cortical TMS effects

Konstantin Weise[1,2+*], Ole Numssen[3+], Axel Thielscher[4,5], Gesa Hartwigsen[3#], Thomas R. Knösche[1,6#]

1Max Planck Institute for Human Cognitive and Brain Sciences, Stephanstr. 1a, 04103 Leipzig, Germany.

2Technische Universität Ilmenau, Advanced Electromagnetics Group, Helmholtzplatz 2, 98693 Ilmenau, Germany.

3Lise Meitner Research Group "Cognition and Plasticity", Max Planck Institute for Human Cognitive and Brain Sciences, Stephanstr. 1a, 04103 Leipzig, Germany.

4Danish Research Centre for Magnetic Resonance, Centre for Functional and Diagnostic Imaging and Research, Copenhagen University Hospital Hvidovre, Denmark.

5Technical University of Denmark, Center for Magnetic Resonance, Department of Health Technology, Kongens Lyngby, Denmark.

6Technische Universität Ilmenau, Institute of Biomedical Engineering and Informatics, Gustav-Kirchhoff-Straße 2, 98693 Ilmenau, Germany.

+,# contributed equally

* CORRESPONDING AUTHOR

Konstantin Weise; Max Planck Institute for Human Cognitive and Brain Sciences, Stephanstr. 1a, 04103 Leipzig, Germany; Technische Universität Ilmenau, Advanced Electromagnetics Group, Helmholtzplatz 2, 98693 Ilmenau, Germany; e-mail: kweise@cbs.mpg.de, phone: +49 341 9940-2580

26 **ABSTRACT**

27 Despite the widespread use of transcranial magnetic stimulation (TMS), the precise cortical

28 location underlying the physiological and behavioral stimulation effects are still only coarsely

29 known. So far, mapping strategies rely on center of gravity approaches and therefore localize

30 the stimulated cortical site only approximately and indirectly. Focusing on the motor cortex, we

31 present a novel method to reliably determine the effectively stimulated cortical site at the

32 individual subject level. The approach combines measurements of motor evoked potentials

33 (MEPs) at different coil positions and orientations with numerical modeling of induced electric

34 fields. We identify sharply bounded cortical areas around the gyral crowns and rims of the

35 motor hand area as the origin of MEPs and show that the tangential component and the

36 magnitude of the electric field is most relevant for the observed effect. To validate our

37 approach, we determined motor thresholds for coil positions and orientations for the predicted

38 cortical target. Our methods allows for the identification of optimal coil positions and

39 orientations. Moreover, we used extensive uncertainty and sensitivity analyses to verify the

40 robustness of the method and identify the most critical model parameters. Our generic

41 approach improves the localization of the cortex area stimulated by TMS and may be

42 transferred to other modalities such as language mapping.

43

44

48

49 **1 INTRODUCTION**

50 Transcranial magnetic stimulation (TMS) is capable of modulating motor and cognitive

51 functions in the human brain. An important application of this technique is mapping structure-

52 function relationships (see Bestmann and Feredoes, 2013; Sandrini et al., 2011; Siebner et al.,

53 2009 for review). Answering the question of *"which part of the brain gets stimulated, and how*

54 *do we know where it is?"* on the individual subject level is essential to understand brain

55 physiology and structure function relationships. Such mappings are not only of fundamental

56 neuroscientific interest, but also have practical clinical relevance, for example in the context of

57 pre-surgical mapping for counseling and planning tumor resections or epilepsy surgeries. In a

58 classical mapping study, the TMS coil is systematically moved over different positions and/or

59 orientations while certain behavioral or physiological variables (e.g., the degree of speech

60 impairment or the magnitude of motor evoked potentials) are measured (Picht, 2014). The coil

61 position/orientation producing the strongest effect is then used as a proxy for the brain

62 structures underlying the targeted effects, either in a simple way by direct projection onto the

63 cortical surface (Krieg et al., 2014) or in a more sophisticated way by calculating the induced

64 electric fields (Tarapore et al, 2013). However, this approach has some principal shortcomings.

65 First, its capability to unambiguously determine the location and orientation of stimulated

66 neural structures is limited: even if the coil configuration associated with the optimal effect can

67 be found accurately, this coil configuration generates electric fields in a wide range of neural

68 structures, such as radial cells in several parallel sulcal walls and tangential structures (e.g.,

69 axons) in gyral crowns. The field maximum does not reliably indicate which of these

70 components is actually driving the effect. Second, as the search space has at least three

71 dimensions (two for the position on the head surface, one for coil orientation), accurate

72 mapping may require a very large number of stimulations to avoid undersampling.

73 Consequently, previous studies remain controversial on fundamental aspects of the

74 physiological TMS effects and their localization on the cortical surface. For instance, it is still

75 unclear which part of the primary motor cortex is effectively stimulated by the TMS pulse (see

76 Bungert et al., 2017; Laakso et al., 2018; Fox et al., 2004; Krieg et al., 2013), precluding

77 strong conclusions on the cortical origin of the TMS effect. In particular, previous studies

78 remain controversial with respect to the contribution of the gyral crowns and sulcal walls in the

79 primary motor cortex (see Fox et al., 2004; Bungert et al., 2017; Opitz et al., 2013; Laakso et

80 al., 2018; Krieg et al., 2013).

81 Resolving these limitations and establishing a link between coil position and location and size

82 of affected cortical area in three dimensions (i.e., also in depth) is not trivial. It requires

83 detailed knowledge of the electric field pattern at the individual level, biophysically motivated

84 hypotheses on the mechanism of action by which the electric field causes neural excitation,

85 and formal statistical testing to demonstrate the validity of the obtained results.

86 The induced electric field distribution strongly depends on several stimulation parameters such

87 as intensity, location, and orientation of the TMS coil as well as the complex geometry of the

88 individual brain (Thielscher et al., 2011), and several biophysical parameters, such as tissue

89 conductivities and fractional anisotropy. Numerical modeling of the induced electric field is

90 increasingly being increasingly used to address these issues (Bestmann, 2015; Thielscher et

91 al., 2011; Thielscher et al., 2015), but has not become a standard procedure in medical and

92 scientific applications so far. In particular, calculations based on subject-specific head meshes

93 have improved our understanding of the impact of individual head anatomy on field

94 distributions (Datta et al., 2010; De Lucia et al., 2007; Opitz et al., 2013; Opitz et al., 2011;

95 Opitz et al., 2014; Thielscher et al., 2011). As such, numerical field calculations using

96 anatomically detailed head models may assist the neurobiological interpretation of TMS effects,

97 and aid the localization of the stimulated cortical area that underlies the observed physiological

98 or behavioral effect (see Hartwigsen et al., 2015; Bungert et al., 2017). However, since a TMS

99 pulse induces a distributed electric field over an extended part of the cortex, it is difficult to

100 determine the location of neural activation, even if the field is computed in a reliable way.

101 Moreover, any approach that aims to make beneficial use of field models has to account for the

102 uncertainties of the numerical simulations to yield accurate and robust conclusions.

103 Uncertainties are particularly caused by the assumed ohmic tissue conductivities, which are

104 only coarsely known. Such an approach also has to be further able to deal with uncertainties

105 caused by the limited knowledge on how the induced field acts on different neuron types.

106 Recently, field calculations have been combined with microscopic neural models based on

107 accurate reconstructions from histology (Seo et al., 2017; Aberra et al. 2018). However, for

108   now, validation of these models is still largely missing to a large extent and the conclusions

109   strongly depend on model details such as the types of the included neural elements.

110   Consequently, the results of previous studies strongly differ and do not provide reliable

111   conclusions yet.

112   In this study, we introduce a novel TMS mapping approach that links biophysical modeling of

113   the induced electric field with physiological measurements within a principled statistical testing

114   framework to determine the stimulated cortical area on the individual subject level. Our

115   approach is based on the assumption of a unique functional relationship between the observed

116   physiological TMS effect and the electric field induced at the cortical location underlying this

117   effect. Given an experimental effect that linearly or non-linearly scales with stimulation

118   intensity, one can assume that this effect also scales with the degree of excitation of the

119   specific neuronal population, which is functionally linked to it. Hence, the functional

120   relationship between the electric field component that coincides spatially and orientation-wise

121   with this population and the observed effect should be invariant across experimental

122   conditions, that is, different orientations and positions of the TMS coil. Consequently, the

123   stimulated cortical area can be localized by determining the brain area in which the induced

124   field shows a clear functional relationship between the measured effects across conditions.

125   Note that this area does not have to coincide with the field maximum. Similar, but more

126   restricted, localization approaches were used in previous studies. For instance, targeting the

127   hand area of the primary motor cortex, Bungert et al. (2017) employed a statistical approach

128   based on the experimentally determined motor thresholds at different coil orientations. Laakso

129   et al. (2018) used a similar strategy, but investigated the influence of different coil positions

130   while keeping the orientation constant. These studies demonstrate the principal validity of the

131   rationale to localize the stimulated cortical area using the functional relationship between

132   calculated fields and the observed effects. However, they remain restricted in several

133   important aspects. First, the ability for a precise functional localization at the single-subject

134   level was not demonstrated. Second, it remains unknown how many experimental conditions

135   are needed to achieve a satisfying localization result and how these coil positions and

136   orientations should be chosen. Third, the robustness of the approaches to uncertainties of

137   tissue conductivities was not examined. Finally, all of the aforementioned publications lack

138 experimental validation.

139 Our novel approach differs from these prior studies in two important aspects to advance

140 localization at the single-subject level: 1) it combines multiple stimulations with different coil

141 positions and orientations. 2) Instead of relying on motor threshold, it exploits entire input-

142 output curves (I/O curves; relationship between stimulation intensity and MEP amplitude; see

143 Fig. 1). We show that our method provides a means of precisely localizing the individual

144 cortical area that is responsible for the observed motor output. We prove its stability and

145 robustness using comprehensive permutation tests and a rigorous uncertainty and sensitivity

146 analysis based on the generalized polynomial chaos (gPC) approach (Le Maitre et al., 2010).

147 To account for the limited knowledge on the neural target structures of TMS, we tested several

148 components of the induced field, and consistently found the tangential field component and the

149 field magnitude to be the relevant quantities for modulating the observed effect. Importantly,

150 we demonstrate that unique results can be obtained with relatively few measurements and

151 indicate how the respective coil positions and orientations should be chosen. We validated our

152 method by numerically optimizing the individual TMS coil position and orientation to effectively

153 stimulate the identified cortical targets. These coil positions and orientations were shown to

154 produce lower MTs than any other tested coil configuration. Our approach improves the

155 localization of effectively stimulated areas during TMS. While demonstrated for the motor

156 cortex, our approach is generic and can be applied to mapping procedures in other domains

157 such as language.

158 **2 MATERIALS AND METHODS**

159 We developed a novel framework to localize the neuronal populations that are responsible for

160 effects of TMS by combining behavioral responses with numerical modeling. We applied this to

161 primary motor cortex stimulation and electrophysiological measurements of muscle activation.

162 First, we describe the experimental design to elicit and measure MEPs (2.1). Second, we show

163 how to calculate the TMS induced electric field distribution in the subjects' heads (2.2). This

164 covers models for the head, the TMS coils, as well as the differential equations numerically

165 solved to determine the electric field inside the brain. Third, we present a new measure to

166 quantify the correlation between the induced electric field and the behavioral or physiological

167 stimulation effect, the *congruence factor*. Locations with high congruence are likely to house

168 neural populations that are causally linked to the observed MEP (2.3). We then show how the

169 results are analyzed in terms of their sensitivity towards uncertain model parameters such as

170 the electrical conductivities of the brain tissues and the measured MEPs using a generalized

171 polynomial chaos (gPC) approach (2.4). Finally, the validation procedure for our results is

172 outlined (2.5).

173 **2.1 TMS Experiments**

174 The experimental setup is shown in Fig. 1. Fifteen healthy, right-handed participants (seven

175 female, age 22-34 years) with a mean laterality index of 92.93 (SD = 10.66) according to the

176 Edinburgh Handedness Inventory were recruited. Subject inclusion was in accordance with the

177 published safety guidelines on patient selection for TMS studies (Rossi et al., 2009; Rossini et

178 al., 2015). Written informed consent was obtained from all participants prior to the

179 examination. The study was performed according to the guidelines of the Declaration of

180 Helsinki and approved by the local Ethics committee of the Medical Faculty of the University of

181 Leipzig.

182 Stimulation was applied with a MagPro X100 stimulator (MagVenture, firmware Version 7.1.1)

183 and CB-60 figure-of-eight coils, guided by a neuronavigation system (software: Localite,

184 Germany, Sankt Augustin; camera: Polaris Spectra, NDI, Canada, Waterloo).

185 MEPs were recorded from the subjects' right hand index finger with one surface electrode

186 positioned over the muscle belly of the FDI and one at the proximal interphalangeal joint (PIP).

187 The electrodes were connected to a patient amplifier system (D-360, DigitimerLtd., UK,

188 Welwyn Garden City; bandpass filtered from 10 Hz to 2 kHz), which in turn was connected to a

189 data acquisition interface (Power1401 MK-II, CED Ltd., UK, Cambridge, 2 kHz sampling rate).

190 Stimulation control and recording was performed with Signal (CED Ltd., version 4.11).

191 Localization of the MEP stimulation hotspot was guided by individually transformed M1

192 coordinates based on the standardized group coordinates from a meta-analysis (Mayka et al.

193 2006). These coordinates were transformed to the individual subject's space by using the

194 inverse of the normalization transformation in SPM (Penny et al., 2007;

195 https://www.fil.ion.ucl.ac.uk/spm/). The individual MEP producing hotspot $M1_{45°}$ and its

196   corresponding resting motor threshold ($MT_{M1_{45°}}$) were determined. $MT_{M1_{45°}}$ was defined as the

197   minimum stimulation intensity, which evokes MEPs with an amplitude of at least 50 μV in at

198   least 5 out of 10 consecutive stimulations (Pascual-Leone and Torres, 1993; Rothwell et al.,

199   1999; Conforto et al. 2004).

200
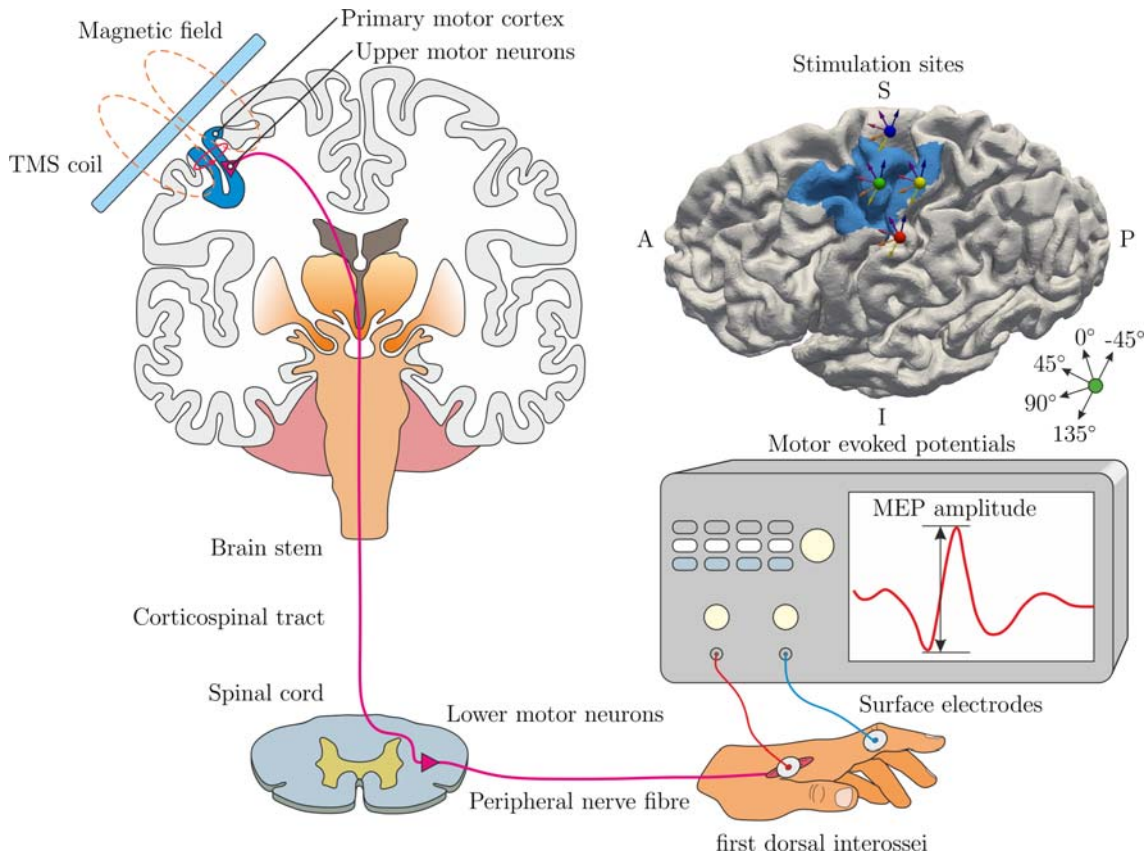
Figure 1: Schematic representation of the experimental procedure of the TMS experiments. Top left: The
TMS coil is located tangentially to the skull over the primary motor cortex (M1). A time changing current
in the coil generates a time changing magnetic field, which induces an electric field in the brain. This
depolarizes the upper motor neurons with corticospinal efferents. Bottom: Action potentials from the
upper motor neurons excite the lower motor neurons in the spinal cord, evoked action potentials travel
through the peripheral nerves to the first dorsal interossei (FDI) of the hand. Sum potentials (motor-
evoked potentials, MEP) are recorded from hand muscles using a classical belly tendon montage, i.e.
between the dorsal interosseus and proximal interphalangeal joint of the index finger. Top right: example
cortical surface with region of interest (blue), showing positions of the coil centers (colored spheres) and
the coil orientations (arrows) for the 20 experimental conditions.

211   In relation to M1$_{45°}$, five additional conditions, shown in Fig. 2(a), with different stimulation

212   sites and coil orientations (see Fig.2a) were defined in the following way: in Experiment I, the

213   TMS coil was located over M1 and 2 cm posterior (P). At both sites, three coil orientations with

214   respect to M1$_{45°}$ were investigated, namely M1$_{0°}$/P$_{0°}$ (-45° from M1$_{45°}$), M1$_{45°}$/P$_{45°}$, and

215   M1$_{90°}$/P$_{90°}$ (+45° from M1$_{45°}$), resulting in six experimental conditions.

216   Experiment II included three of the subjects from Experiment I and the number of conditions

217   was increased to further investigate the influence of different coil positions and orientations on

218   the determination of the effective stimulation site. In addition to M1 and P, two more coil

219   positions were included, shown in Fig. 2(b), 2 cm inferior and 2 cm superior to M1,

220   respectively (Fig.2b). For each position, the number of coil orientations was increased to 5 (-

221   90°, -45°, 0°, 45°, 90°) with respect to $M1_{45°}$, resulting in 20 experimental conditions.
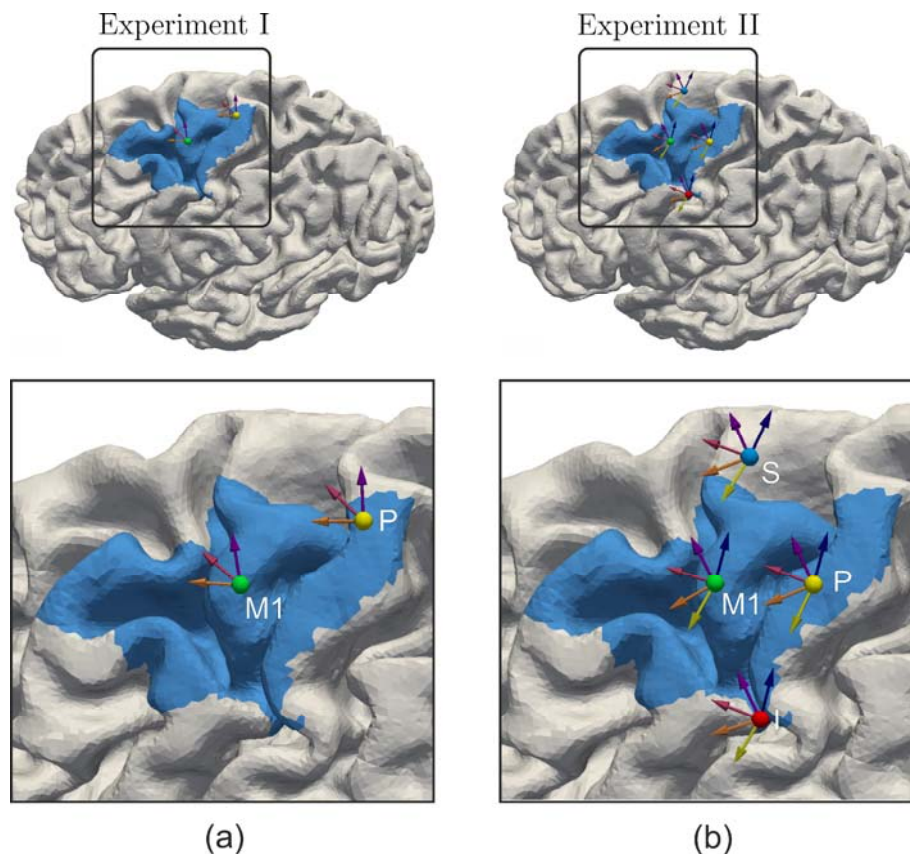

222

223   **Figure 2:** Coil positions and orientations used in (a) Experiment I and (b) Experiment II. The locations
224   are exemplarily shown for subject S8. The number of experimental conditions increases from six to 20.
225   The blue area is the region of interest, comprised of the somatosensory cortex S (BA 1, BA 3), M1 (BA 4),
226   and the dorsal part of the premotor cortex (BA 6).

227   In both experiments, single biphasic pulses with an inter stimulus interval of 5 s (Experiment

228   I) or 4 s (Experiment II) were applied for each condition. The coil positions/orientations were

229   recorded by the neuronavigation system. The MEPs were lowpass filtered with a 6th order

230   Butterworth filter with a cutoff frequency of 500 Hz. Afterwards, the peak-to-peak amplitudes

231   of the MEPs were calculated in a time window of 18 to 35 ms after the TMS pulse (see Fig 3a

232   for an example MEP). Stimulation intensities were chosen to sample the complete I/O curve for

233 each experimental condition, unless maximal stimulator output was reached before (Fig. 3(b)).

234 Intensity was increased in steps of 2% stimulator output (MSO), or 1% respectively for

235 intensity ranges of high I/O gradients (cf. Bungert et al., 2017). For each intensity, 3-5

236 stimulations were performed to determine an average MEP amplitude. Trials with deviations in

237 coil position of ±3 mm and orientation of ±5° with respect to each axes were removed. A

238 typical set of data points is shown in Fig. 3(b) (blue dots). Thereafter, a sigmoidal function was

239 fitted in a least-square sense:

$$s_i(x) = \frac{a_i}{1+e^{-b_i(x-x_{0,i})}},$$
(1)

240 where a_i is the saturation amplitude, b_i the slope, and $x_{0,i}$ is the location of the turning point on

241 the abscissa. If only a part of the I/O curve could be determined experimentally, a sigmoidal

242 function could not be reliably fitted and an exponential or linear function was used instead. The

243 selection of the optimal model was performed using the Akaike information criterion (AIC,

244 Akaike, 1974). The procedure was repeated for all experimental conditions (i.e., for different

245 coil positions and orientations) in a pseudo-randomized order.
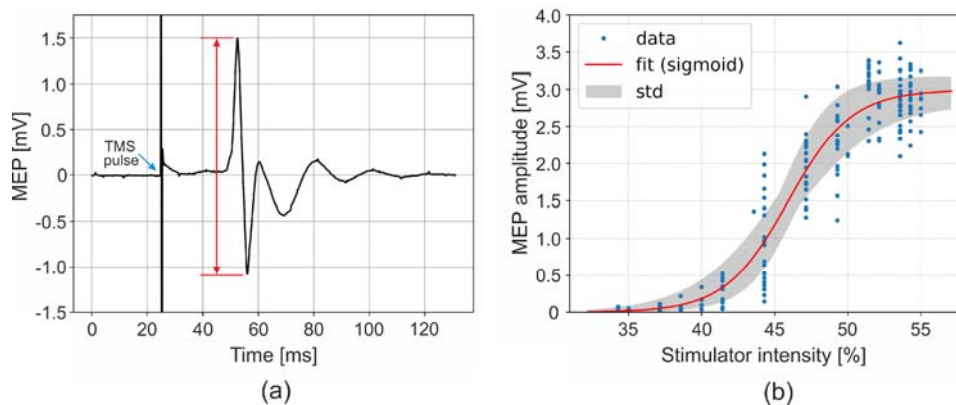
246

247 **Figure 3**: (a) Measured motor evoked potential (MEP) showing the stimulation artifact (blue arrow) and
248 highlighting the peak-to-peak amplitude (red arrow). (b) I/O curve characterizing the MEP amplitudes as
249 function of the stimulator intensity for one experimental condition. Blue dots: MEP amplitudes for the
250 different stimulator intensities. Red curve: fitted analytical function. Depending on the best Akaike
251 information criterion (AIC), MEP amplitudes were fitted to sigmoidal, exponential or linear functions
252 (presented example: sigmoid function). Black lines: possible I/O curves resulting from uncertainty in the
253 experimental data.

254 **2.2 Numerical simulations of the induced electric field**

255 The calculations of the electric field were conducted with SimNIBS v2.0 (Thielscher et al.,

256 2015) using high-resolution anisotropic finite element models (FEMs), as exemplary shown for

10

257 one subjects in Fig. 4. The individual head models were generated from MRI data using the

258 pipeline described in Windhoff et al. (2013), employing FreeSurfer

259 (http://surfer.nmr.mgh.harvard.edu/, Dale et al., 1999; Fischl et al., 1999) and FSL

260 (https://fsl.fmrib.ox.ac.uk/fsl/fslwiki/FSL, Woolrich et al., 2009; Smith et al., 2004; Jenkinson

261 et al., 2012). The head models were composed of ~$1.3 \cdot 10^6$ nodes and ~$7 \cdot 10^6$ tetrahedra. T1

262 and T2 images were used for segmenting the main tissues of the head: scalp, skull, grey

263 matter (GM), white matter (WM), and cerebro-spinal fluid (CSF). Diffusion weighted images

264 were used to reconstruct the conductivity tensors in the WM using the volume normalized

265 mapping approach (Güllmar et al., 2010). To this end, the following structural images were

266 acquired with a 3 Tesla MRI scanner (Siemens Verio or Skyra) and a 32 channel head coil. The

267 following images were acquired: (i) T1-weighted: MPRAGE with 176 sagittal slices, matrix size

268 = 256 x 240, voxel size = 1 x 1 x 1mm³, flip angle 9°, TR/TE/TI = 2300/2.98/900ms

269 (Repetition, Spin echo, Inversion Time), (ii) T2-weighted: 192 sagittal slices, matrix size = 256

270 x 258, voxel size = 0.488 x .488 x 1mm³, flip angle 120° TR/TE = 5000/395ms (iii) diffusion

271 MRI (67 axial slices, matrix size 128 x 128, voxel size 1.71875 x 1.71875 x 1.7mm³, TE/TR

272 80/7000ms, flip angle 90°, 67 diffusion directions, b-value 1000s/mm³. An additional b0

273 image with reversed encoding direction was recorded for distortion correction with FSL topup

274 and eddy. The T1 image was also used for neuronavigation during TMS. If adequate scans (age

275 less than 1 year) already existed for the subjects in the image database, these scans were

276 utilized.

277 All TMS coils were individually modelled by magnetic dipoles based on X-ray images. Coil

278 wiring differences (shifts of several millimeters and tiltings of about 2-5°) were observed and

279 accounted for. Each coil model consisted of ~4500 magnetic dipoles. These dipole models were

280 compared to a detailed current density based FEM model using Comsol Multiphysics v4.4

281 (COMSOL, Inc., Burlington, MA, USA) and yielded magnetic field errors of < 0.1% at a distance

282 of 15 mm.

283 The magnetic field produced by the coil was calculated in advance in terms of the magnetic

284 vector potential A. The primary electric field is then given by $E_p = -j\omega A$, where $\omega = 2\pi f$ is the

285 angular frequency of the biphasic TMS pulse. The electric potential ϕ in the nodes is calculated

286   by solving the Laplace equation $\nabla \cdot ([\sigma] \nabla \phi) = 0$, considering anisotropic conductivity tensors $[\sigma]$

287   inside each element together with the boundary conditions given by the law of current

288   conservation $\nabla \cdot J = 0$. After calculating the secondary electric field $E_s = -\nabla \phi$, the total induced

289   electric field is given by $E = -j \omega A - \nabla \phi$. The conductivity values for the five examined tissues

290   ($\sigma_{Scalp} = 0.465$ S/m, $\sigma_{Skull} = 0.01$ S/m, $\sigma_{GM} = 0.275$ S/m, $\sigma_{WM} = 0.126$ S/m, $\sigma_{CSF} = 1.654$ S/m) were

291   taken from Thielscher et al. (2011) and Wagner et al. (2004). A more detailed description

292   about the FEM solver is given in Windhoff et al. (2013, supplemental material).

293   Individual coil positions and orientations relative to the subject's head were saved by the

294   neuronavigation system for each stimulation. These coil configurations were used for electrical

295   field calculations in SimNIBS. A region of interest (ROI) was defined covering the

296   somatosensory cortex (BA 1, BA 3), M1 (BA 4), and the dorsal part of the premotor cortex (BA

297   6) with Freesurfer and a mask was created for the Freesurfer average template and

298   transformed to each individual subject's brain.
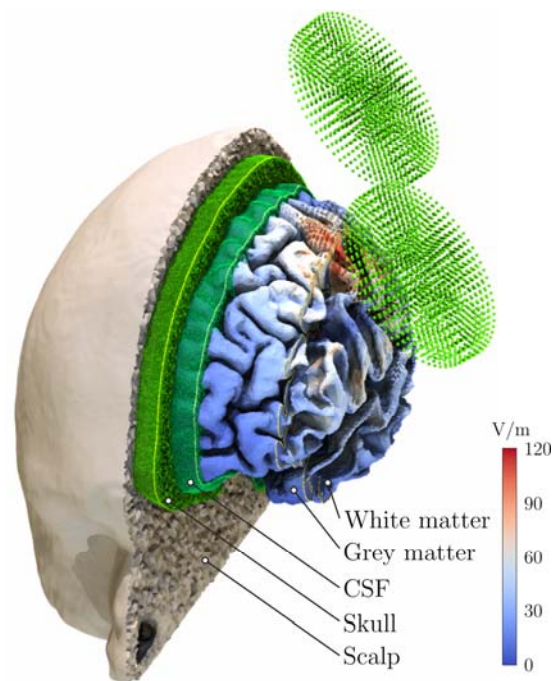
299

300   **Figure 4:** Example of the realistic anisotropic head model of one subject, used for the numerical
301   simulations of the induced electric field. The model consists of $1.26 \cdot 10^6$ nodes and $7.12 \cdot 10^6$ tetrahedra.
302   The TMS coil is modeled using 4440 magnetic dipoles (green spheres) with optimized dipole moments
303   located in five layers. The grey matter surface is color coded with the magnitude of the induced electric
304   field for 1 A/μs intensity.

12

305   The following analyses were performed on the midlayer between the outer surfaces of the GM

306   and WM compartments in order to avoid boundary effects of the electric field due to

307   conductivity discontinuities. The electric field was interpolated in the nodes of this surface in a

308   post-processing step. Fig. 5 shows the magnitude $|E|$, the normal component $|E_\perp|$ and the

309   tangential component $|E_\parallel|$ of the electric field at the midlayer surface for three different coil

310   positions and orientations in one exemplary subject. The different electric field distributions are

311   shown in the highlighted ROI for the different experimental conditions.
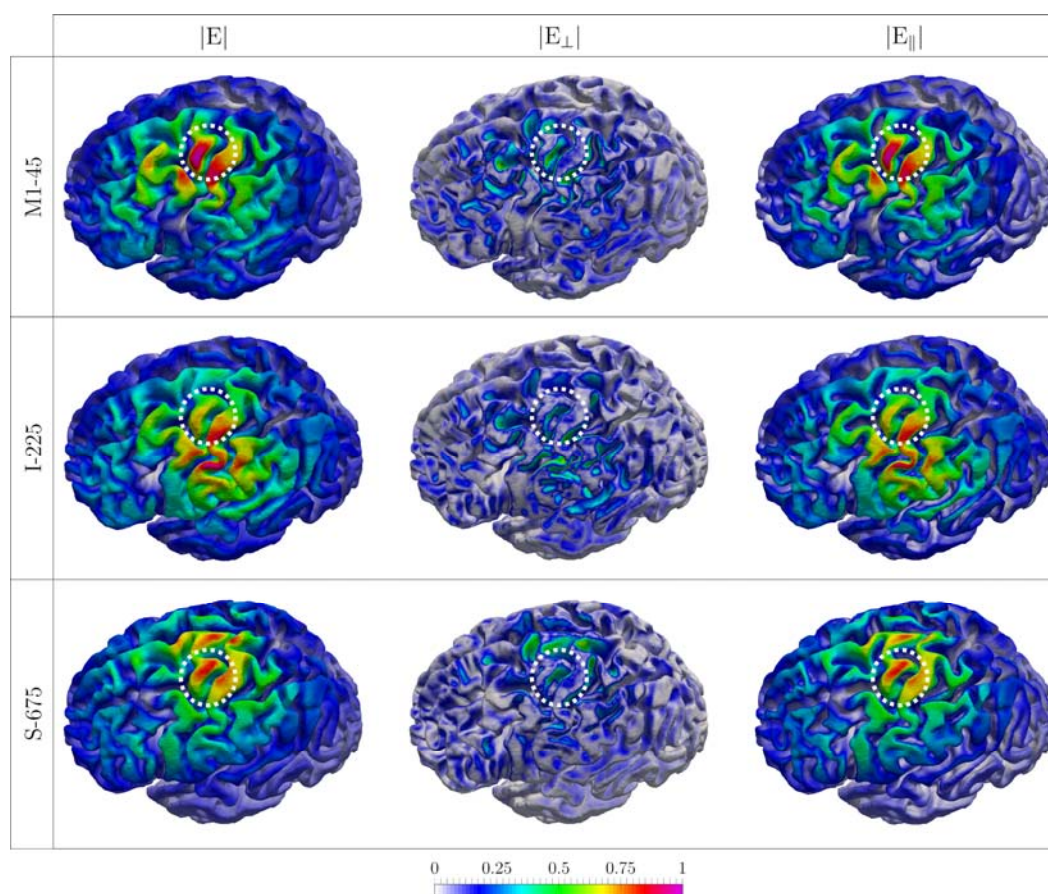
312

313   **Figure 5:** Three electric field distributions, i.e. the magnitude of the electric field $|E|$, the normal

314   component $|E_\perp|$, and the tangential component $|E_\parallel|$ for one exemplary subject. The electric field was

315   normalized to allow comparability between the different experimental conditions. The white circle shows

316   the M1 hand knob area.

2.3 Determining the site of stimulation

318   The core concept of the proposed method is illustrated in Fig. 6. We assume that at the site

319   of activation the correlate between electric field and MEP is stable, i.e. the same electric field

320   evokes the same behavioral output independent of the location or orientation of the TMS coil.

321   Exploiting this property, we can single out the site of stimulation can be singled out by

322   calculating *cortical I/O curves* that represent the relationship between the electric field in the

323   cortex and the resulting MEP, and then comparing the cortical I/O curves of the different

324   experimental conditions. At the true cortical site of stimulation, the I/O curves of all conditions

325   should be similar. Practically, this was achieved by transforming the measured I/O curve for

326   each condition (representing the relationship between stimulation intensity in percent of

327   maximal stimulator output, %MSO, and MEP amplitude) to E-MEP-curves (representing the

328   relationship between the electric field at a particular cortex location and the respective MEP

329   amplitude). The electric field distribution throughout the brain was computed as a function of

330   the stimulation intensity using the numerical techniques described above, thereby taking 100%

331   MSO as corresponding to a maximal change of the coil current of 140 A/µs for the used

332   stimulator-coil combination. Due to the linear relationship between electric field strength and

333   stimulator intensity, the E-MEP curves were shifted and horizontally scaled versions of the

334   measured I/O curve, with different shift and scale parameters in each position. Hence, the

335   function types of each I/O curve and their corresponding E-MEP curves are similar (i.e.

336   sigmoidal, exponential, or linear). E-MEP curves can be determined for all different

337   components of the electric field vector ($|E|$, $|E_\perp|$, $|E_{||}|$) or, in principle, any other derived

338   quantities thereof. This approach allows computing a position-wise *congruence factor* $c(r)$,

339   which quantifies the similarity between the E-MEP curves of the different experimental

340   conditions.

341   The agreement between different I/O curves was quantified by computing the inverse

342   variance of the optimal shifts τ_i with $i = 1 \dots N_c$ of the N_c I/O curves across the experimental

343   conditions.

$$c(r) = \left(\frac{1}{N_c} \sum_{i=1}^{N_c} \frac{\left(\underline{\tau}(r) - \tau_i(r) \right)^2}{\overline{\mathrm{E}}^2(r)} \right)^{-1} \qquad (1)$$

344   The congruence factor $c(r)$ was calculated in each element in the ROI on the cortex by

345   determining the inverted variance of the τ_i, additionally weighted by the average electric field

346   magnitude (or its normal or tangential component) squared at this location: $\overline{\mathrm{E}}^2(r)$. Hence, the

347   congruence factor quantifies a relative similarity between the observations in the different

348 experimental conditions independent on the scale of the electric field. Higher similarity

349 between curves leads to higher inverse variance. The optimal shifts τ_i were obtained by

350 determining the individual locations where the overlap against a reference curve, e.g. the first

351 E-MEP curve, is maximized. As a result, the problem of determining the congruence factor

352 turns into many optimization problems to calculate the shifts τ_i for each condition and in each

353 element in the ROI:

$$\min_{\tau_i} \| s'_{REF}\big(E(r)\big) - s'_i(E(r) - \tau_i) \|_2 \qquad (2)$$

354 Where s'_{REF} and s' denote the reference and one of the I/O curves the shift is calculated for,

355 respectively. This method is very general, as it is independent of the involved function types.
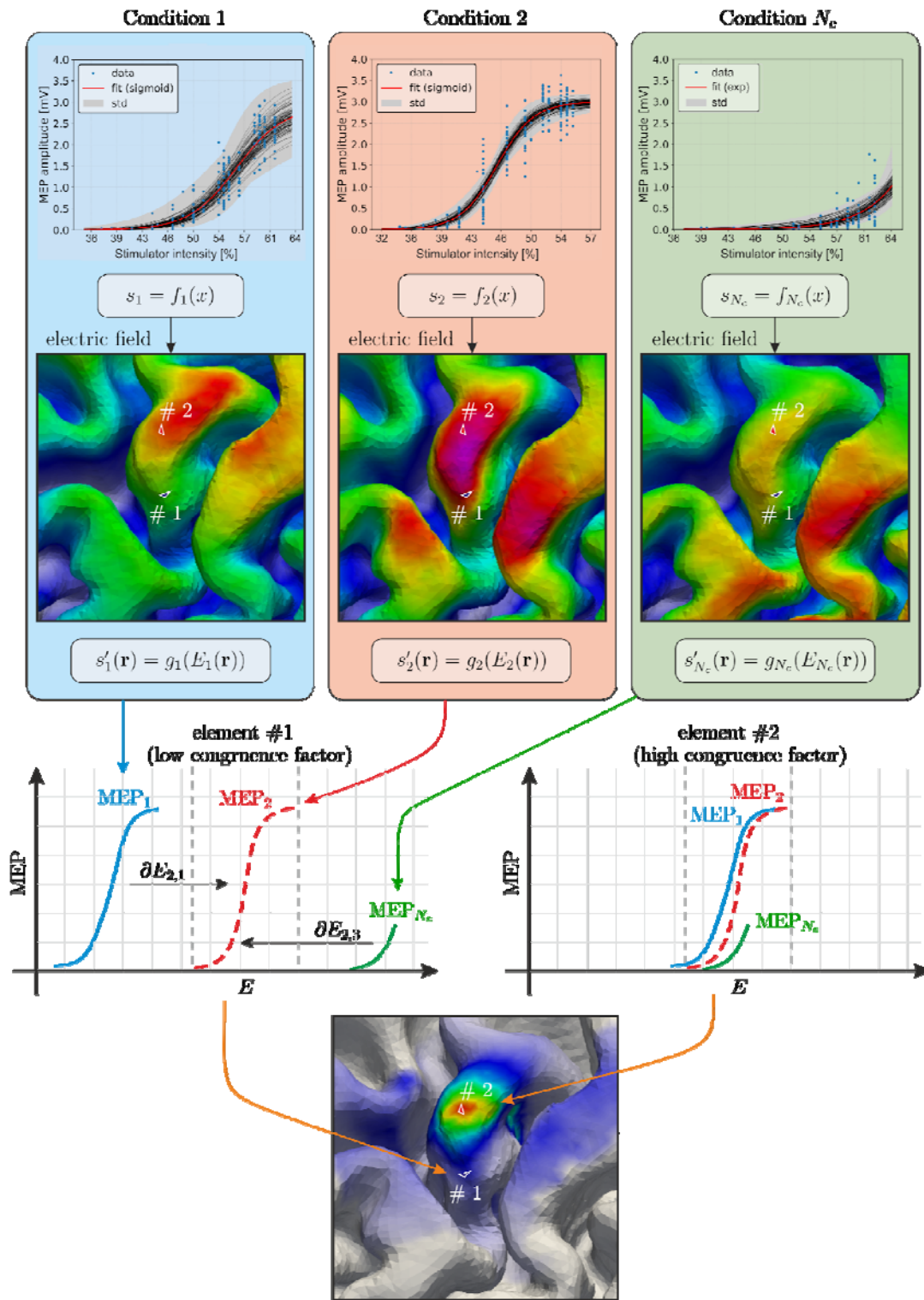
Figure 6: Principled approach to determine the site of stimulation by TMS. The *congruence factor* is based on the assumption that the electric field, which is causal to the observed behavioral effect, corresponds for the experimental conditions. The measured I/O curves are transformed to element wise E-MEP-curves using electromagnetic field modeling (see text). The congruence factor between the E-MEP-curves inversely depends on the amount of transformation (shift) necessary to obtain maximum overlap between the E-MEP-curves in each element.

363   Because the electric field scales the I/O curves linearly, eq. (2) can be reformulated in terms of

364   stimulator intensity, which allows a highly efficient implementation. A more detailed

365   mathematical description is given in Section 1.2 of the *Supplementary Material*.

366   This is beneficial if the experimentally determined I/O curves capture only a linear or

367   exponential part of the relationship between electric field and MEP amplitude (see above). If,

368   however, each E-MEP curve can be represented as analytical sigmoidal function, parameterized

369   by its turning point $x_{0,i}$, the shifts τ_i are directly given by $\tau_i = x_{0,i}E_i(r)$ and the computational

370   expensive optimization from eq. 2 is avoided, thus making the method computationally very

371   efficient. This approach is advantageous in terms of computational cost and is preferred in the

372   current study if all I/O curves are modelled by sigmoidal functions.

373   As the standard Freesurfer average template (FsAverage) suffers from several malformed

374   elements at the primary motor cortex with each of roughly the 20-fold size as the average

375   elements, we created a group-based average with Freesurfer. In this iterative procedure, a

376   randomly chosen subject was used as initial template and all other subjects were registered to

377   this. In the second step, the template was updated based on these registrations. The third step

378   comprised the registration of all subjects to this updated template. The second and third steps

379   were then repeated to improve the template.

380   **2.4 Uncertainty and sensitivity analysis**

381   The congruence factor is influenced by several parameters. For example, previous studies have

382   shown that, because of their large uncertainties, the electrical ohmic conductivities of brain

383   tissues have a strong influence on the magnitude of the electric field (Weise et al., 2015;

384   Codecasa et al., 2016). Furthermore, the estimated parameters of the fitted MEP curves are

385   also uncertain due to measurement noise (Fig. 3b, grey interval). Therefore, uncertainty and

386   sensitivity analyses are important to investigate the stability of the results and identify the

387   parameters and their combinations with the largest impact on the results.

388   Since the problem is computationally complex and features a large number of parameters p,

389   an efficient approach is necessary to conduct the analysis. Here, we applied the generalized

390   polynomial chaos (gPC) method (Ghanem et al., 2016). Its mathematical background is

391   described in detail in Section 1.3 of the *Supplemental Material*. In short, the gPC is based on

392 the construction of a polynomial surrogate of the congruence factor depending on the

393 uncertain model parameters and their associated probability density functions.

394 **Table 1:** *Limits and shape parameters of the model parameters for subject S1*

Parameter	Description	Min	Max	p / q	Reference / source
σ_{WM}	White matter (WM)	0.1 S/m	0.4 S/m	3 / 3	Li et al. (1968) Nicholson (1965) Akhtari (2010)
σ_{GM}	Grey matter (GM)	0.1 S/m	0.6 S/m	3 / 3	Li et al. (1968) Ranck (1963) Logothetis et al. (2007) Yedlin et al. (1974)
σ_{CSF}	Cerebrospinal fluid (CSF)	1.2 S/m	1.8 S/m	3 / 3	Gabriel et al. (2009) Baumann et al. (1997)
α	Anisotropy scaling	0.4	0.6	3 / 3	Tuch et al. 2001
$x_{0,S(90°)}$*	MEP curve	145.9 [A/µs]	185.9 [A/µs]	4 / 4	experiment
$x_{0,S(135°)}$*	—"—	150.0 [A/µs]	190.0 [A/µs]	4 / 4	—"—
$x_{0,I(45°)}$	—"—	80.7 [A/µs]	87.9 [A/µs]	4 / 4	—"—
$x_{0,I(135°)}$	—"—	125.7 [A/µs]	145.7 [A/µs]	4 / 4	—"—
$x_{0,P(0°)}$	—"—	124.2 [A/µs]	133.3 [A/µs]	4 / 4	—"—
$x_{0,M1(90°)}$	—"—	86.0 [A/µs]	98.7 [A/µs]	4 / 4	—"—

395 *Note: These parameters were considered in the uncertainty and sensitivity analysis to*

396 *determine the site of stimulation by means of the congruence factor. The asterisk marks*

397 *conditions, where only the lower tail of the I/O curve could be determined. These curves are*

398 *subject to a higher measurement uncertainty.*

399 Since the electric field depends on the electrical conductivities [σ] of the brain tissues, the

400 congruence factor will be influenced by varying conductivities as well. The conductivities of GM,

401 WM and CSF were modelled as beta distributed random variables. The impact of the other

402 tissues, like skull and scalp on the electric field was shown to be negligible in previous studies

403 (Weise et al., 2015; Codecasa et al., 2016; Bicalho et al., 2018). However, extending previous

404 studies, the impact of the level of conductivity anisotropy was included in our analysis. The

405 conductivity tensor [σ] for each voxel was derived from the diffusion tensor using the volume

406 normalize approach (Güllmar et al., 2010). This tensor can be visualized as ellipsoid (see Fig.

407 S2). A spherical ellipsoid represents isotropic conductivity with equal conductivity in each

408   direction, while a cigar shaped tensor indicates that the conductivity is much larger in one

409   direction. We implemented an anisotropy scaling factor α that transforms the diffusion tensor

410   from the isotropic case ($\alpha = 0$) via the original tensor obtained from DTI ($\alpha = 0.5$) to a very

411   anisotropic case ($\alpha = 1$). Although, in principle, α could be different in each voxel, this would

412   render the resulting problem intractable. Instead, we assumed that α is the same for all

413   voxels. This reflects systematic errors and uncertainties in the transformation between the

414   diffusion tensor, which depends on the mobility of water molecules, and the conductivity

415   tensor, which represents the mobility of charges. A detailed mathematical description of the

416   parametrization of the fractional anisotropy is given in *Supplemental Material: Section 1.2*.

417   In addition to the conductivity and anisotropy uncertainties, the turning points $x_{0,i}$ from the

418   sigmoidal I/O curves were included in the uncertainty analysis. Their uncertainties were

419   derived from the confidence intervals of the curve fits (cf. Fig. 3b). The stochastic properties of

420   all investigated parameters are summarized in Table 1. The model of the congruence factor

421   used in the gPC based uncertainty and sensitivity analysis is described in detail in

422   *Supplemental Material: Section 1.4*.

423   After deriving the polynomial surrogate using the gPC, the spatial distribution of the

424   expectation $\mu(r)$ and the variance $v(r)$ of the congruence factors $c(r)$ can be calculated. We

425   further analyzed the relative standard deviation $RSD = \frac{\sqrt{v(r)}}{\mu(r)}$ to identify possible parameter

426   ranges, where the congruence factor is primarily influenced. Finally, in the sensitivity analysis,

427   the variance was decomposed into its origins by a Sobol decomposition. The Sobol indices $S_i(r)$

428   represent portions of the total variance $v(r)$, which are due to individual parameters p_i or a

429   combination thereof, e.g. the conductivity of GM or the combination between different

430   measurement parameters (Sobol, 2001; Sudret, 2008).

2.5 Validation

432   To validate the estimated sites of stimulation, we first determined for each of the three

433   subjects of Experiment II the optimal coil position and orientation such that the cortex position

434   at which the electric field maximum was generated coincided with the maximum of the

435   congruence factor. This was done using an exhaustive search optimization procedure, which is

436   described in detail the Supplemental Material 1.5 and will be implemented in the next SimNIBS

437   major release. The identified optimal coil configurations were compared against other

438   neighboring coil configurations by determining the MT at each site. During MT determination,

439   single biphasic pulses with an inter stimulus interval of 5 s were applied. If the determined

440   congruence factor hotspot is indeed the optimal site for stimulation, then the MT should lowest

441   for the optimized coil position/orientation.

3 RESULTS

443   In the following sections, we present the results from Experiment I (15 subjects and 6

444   experimental conditions) and Experiment II (3 subjects and 20 experimental conditions). The

445   latter includes a permutation analysis to determine the number of stimulation sites and

446   corresponding coil positions required to determine the stimulation site reliably. The results

447   from both studies are then compared. Finally, the results of the uncertainty and sensitivity

448   analysis of the congruence factor are presented for one exemplary subject. The most

449   influencing parameters of the numerical model and the experimental data are identified in the

450   ensuing sensitivity analysis.

3.1 Experiment I (15 subjects, 6 experimental conditions)

452   Figure 7 shows the congruence factors of the group average and the 15 individual subjects.

453   The electric field distributions of all conditions were determined for each subject and combined

454   with the fitted MEP curves using the *optimal curve shift approach* because not all MEP curves

455   could be fitted to sigmoidal functions. In 6/15 subjects (marked with an asterisk, *), no I/O

456   curve could be determined for the posterior coil position $P_{0°}$. Hence, the congruence factor was

457   determined using only 5 of the 6 conditions. The congruence factor was calculated for the

458   magnitude ($|E|$), as well as the normal ($|E_\perp|$) and the tangential ($|E_{||}|$) component of the

459   induced electric field. The magnitude and the tangential component reached substantially

460   higher congruence factors and smoother spatial distributions than the normal component

461    $c(|E_\perp|)$. In general, a clear hotspot for $c(|E|)$ and $c(|E_{||}|)$ could be identified in the hand knob

462   area of M1 on the gyral crown of the average template. However, considering the individual

463   congruence factor maps shows that in 7/15 subjects (S1-S7, highlighted in Fig. 7 with a green

464   background) we found clear and unique hotspots only on the gyral crowns in the hand knob

465   area. In 4/15 subjects (S8-S11, Fig. 7, yellow background), we observed a second hotspot in

466   the somatosensory cortex (S1). In 4/15 subjects (S12-S15, Fig. 7, orange background), we

467   could only identify a dominant hotspot in S1. We reason that this is due to array ambiguities,

468   i.e. spurious overlaps, of the realized electric fields and the missing I/O curve of condition $P_{0°}$,

469   in 2/4 and 3/4 subjects of the two groups, respectively. Note that maximum values of the

470   congruence factors substantially differ across subject. This is because small differences in near

471   zero variances among I/O curves may result in large difference in their inverse, that is, the

472   associated congruence factors.

473   We expected that additional experimental conditions, i.e. more coil positions and orientations,

474   would improve the results of the congruence factor towards more plausible hotspot locations in

475   the M1 hand knob area. This hypothesis was investigated in Experiment II by increasing the

476   number of coil positions and orientations from 6 (resp. 5) to 20 (cf. Fig. 2b). We selected one

477   subject out of each of the three result groups described above (S1, S8, and S12) for this
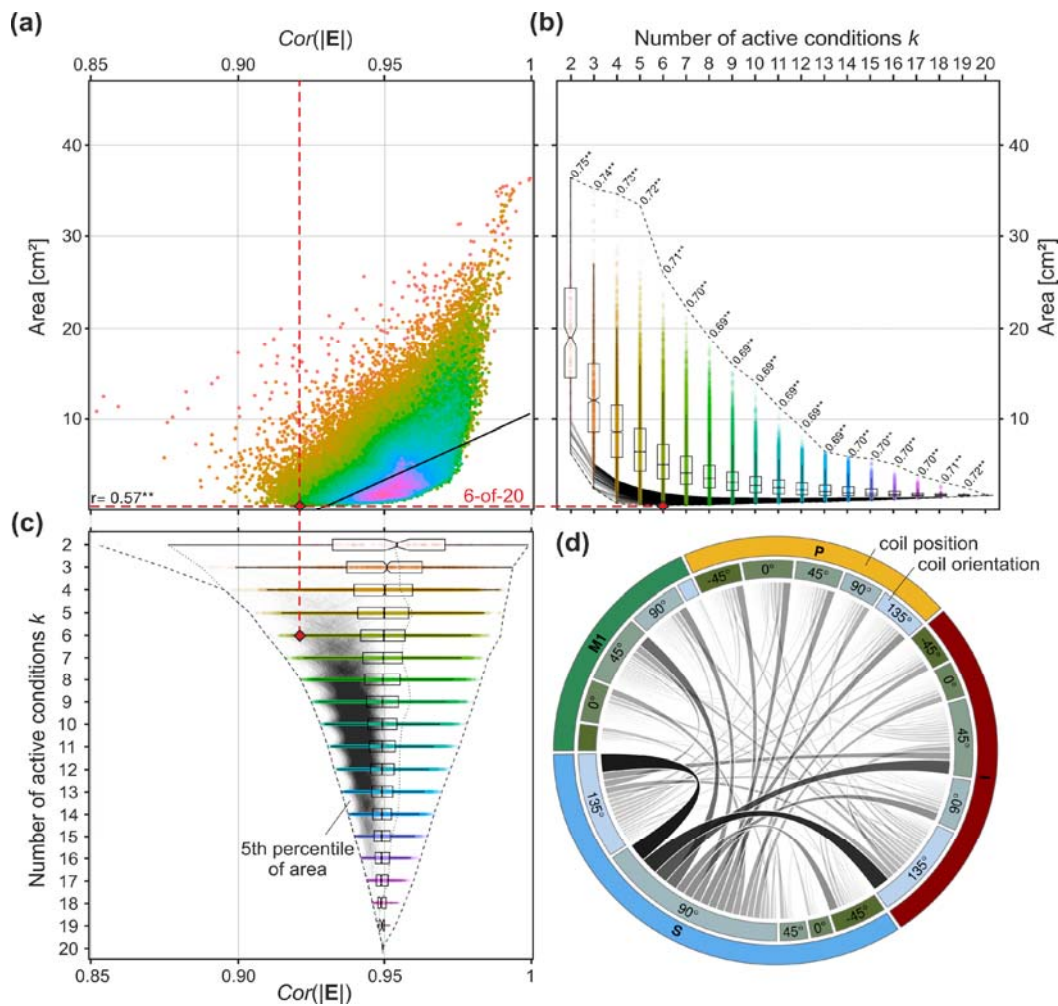
478   experiment.

479
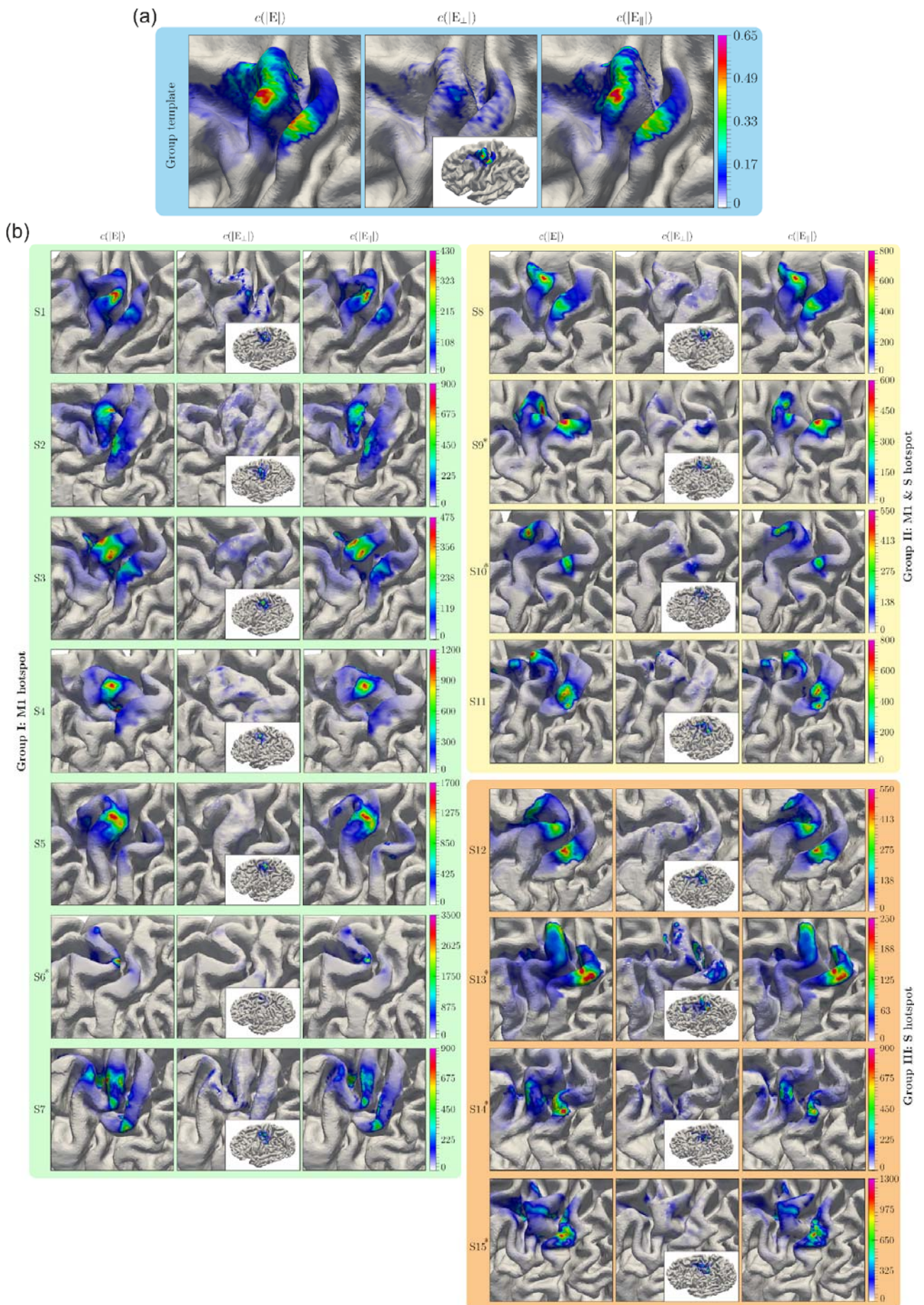
480   **Figure 7:** Congruence factor maps of all 15 subjects including six experimental conditions (Experiment
481   I). The congruence factors were calculated for the magnitude, the normal and the tangential component
482   of the electric field using the optimal curve shift approach. 7/15 subjects show unique hotspots in M1
483   (highlighted in green); 4/15 subjects show hotspots in M1 and S1 (highlighted in yellow) and 4/15
484   subjects show hotspots in S1 only (highlighted in orange); The asterisks (*) mark subjects, where no
485   evaluable MEPs could be determined for the posterior coil position $P_{0°}$. In these cases, the congruence
486   factor was determined using only five conditions; all results were normalized, mapped and superimposed
487   on the group average template shown on the top (highlighted in blue).

488

489   **3.2 Experiment II (3 subjects, 20 experimental conditions)**

490   This experiment was conducted with an extended set of coil positions and orientations

491   (Fig. 2b). For each subject, 20 electric field distributions were calculated and combined with

492   the obtained MEP curves to determine the congruence factor maps. In this experiment, all I/O

493   curves could be fitted to sigmoidal functions, which permits to avoid the computationally

494   expensive optimizations step from (2) by directly using the variance of the turning points.

495   Because 20 experimental conditions are too time consuming to record in future mapping

496   applications based on the proposed method, we investigated how the congruence factor

497   convergences depending on the number of experimental conditions. This enabled us to

498   determine an optimal number and selection of coil positions/orientations to reduce the

499   experimental effort. Consequently a permutation study was performed for each subject by

500   determining the congruence factor for all combinations of $k = 2 \ldots 20$ available experimental

501   conditions. The total number of considered conditions was $\sum_{k=2}^{20} \binom{20}{k} = 1,048,555$. We quantified

502   the focality of each congruence factor map by determining the area with $c > 30$. This threshold

503   was chosen based on the permutation results data to allow comparability between the

504   combinations and subjects. The smaller this area, the more concentrated the map is. That is,

505   the more uniquely the causal relationship between electric field and MEP could be determined.

506

Figure 8: Permutation analysis interrelating the cross-correlation of the electrical fields from the different experimental conditions of Experiment II for subject S1 with the corresponding hotspot area. The hotspot area was defined as the region where $c > 30$. For each case k, the congruence factor was determined $(20\,k\,)$ times. (a) Relationship between the cross-correlation of the electric field magnitude and the resulting hotspot area size. Colors: active conditions k. The correlation coefficient between the hotspot size and the cross-correlation of the electric fields over all k (black line) is $r = 0.57$ $(p \ll .001)$. (b) Boxplot of the hotspot area of the congruence factor depending on the number of active conditions k. Box areas indicate the 25% to 75% quantiles with notch at median. Correlation coefficients between the hotspot size and the cross-correlation of the electric fields for each k are given. ** depict $p < .01$ (after Bonferroni correction). Grey lines: 5th percentile of the best condition combinations for each k. Dashed lines: absolute range. The variation of the hotspot area size decreases with increasing k. (c) Relationship between the cross-correlation coefficient of the electric fields and the number of active conditions k. Box areas indicate the 25% to 75% quantiles with notch at median. Grey lines: 5th percentile of the best condition combinations for each k. Dashed lines: absolute range. The dashed red lines highlight the case of the 6 coil positions and orientations, where the congruence factor map was most focal. Its cross-correlation coefficient is with 0.921 lower than the first quartile of possible solutions. (d) Chord graph highlighting the interaction and relative contribution between different coil positions (outer circle) and coil orientations (inner circle) from the 5th percentile of best condition combinations over all k resulting in small hotspot areas (highlighted with black lines in (b)).

24

524   The results of the permutation study are shown in Fig. 8 for one exemplary subject (S1). The

525   results for the remaining subjects were similar (see Fig. S6 and Fig. S7, respectively). We

526   expected that a lower cross-correlation across the condition-wise electric fields would allow for

527   a higher discriminative power in the determination of the stimulation site. This was confirmed

528   by the analysis in Fig. 8(a), showing a correlation of $r = 0.57$ ($p \ll .001$) between the size of the

529   hotspot area and the cross-correlation of the electric fields over all k. As obvious from the

530   individual number of conditions k, the correlation between the resulting hotspot area and the

531   cross-correlation of the electric fields was stronger for low k (Fig. 8b, correlation coefficients).

532   The median of the hotspot area converges when increasing the number of active conditions.

533   Moreover, the spread of the area decreases by adding more information to the congruence

534   factor calculation. Importantly, the smallest areas (lower dashed line in Fig. 8b) indicates that

535   some condition combinations for $k \geq 5$ result in similar or even smaller areas than for $k = 20$.

536   This shows that the site of stimulation can be determined with relatively few measurements by

537   selecting optimal coil positions and orientations.

538   The relationship between the cross-correlation of the electric fields and the number of active

539   conditions k is shown in Fig. 8c. Cases resulting in the smallest 5th percentile of the hotspot

540   area are shown as thin lines in the shaded area, corresponding to the ones in Fig. 8b. As

541   expected, these cases are concentrated in regions of low cross-correlation.

542   The data were further analyzed to identify which combinations of experimental conditions were

543   especially informative and produce very focal hotspots (Fig. 8d). This analysis was performed

544   for $k = 6$. The appearance of each condition and its co-occurrence with other conditions was

545   accumulated across all condition combinations, which are part of the smallest 5th percentile of

546   the hotspot area (grey shaded area in Fig. 8b). We observed that the co-occurrence was not

547   random and combinations surrounding M1, i.e. inferior, superior, and posterior, appeared more

548   often than coil positions directly over M1. The corresponding coil orientations considerably

549   differed and connections between $S_{90°}$, $S_{135°}$, $I_{45°}$, and $I_{135°}$ stand out. Moreover, it can be

550   observed that posterior conditions occurred frequently in combination with $S_{90°}$, which further

551   confirms the need for highly varying electric field distributions. This behavior is even stronger

552   pronounced for subjects S8 and S12 (cf. Fig. S6 and Fig. S7 in the *Supplemental Material*).

25

553   In the following, the results for $k = 6$ condition combinations out of the 20 experiments (6-of-

554   20) resulting in the smallest hotspot area are described in more detail and compared to

555   Experiment I and to the full 20-of-20 result. The results are shown in Fig. 9 for each subject.

556   The congruence factor maps were normalized with respect to their individual maxima to allow

557   comparability. For subject S1, we already found a unique hotspot in the M1 hand knob area in

558   Experiment I. The results of Experiment II show that this pattern is reproducible and even

559   more focused (as the deflection on the somatosensory cortex is weaker) for the best

560   combination of 6-of-20 conditions. Hence, for this subject, the coil positions of Experiment I

561   were already sufficient to determine the site of stimulation in a plausible manner. The second

562   subject belongs to the group, which showed hotspots in both M1 and S1 (Experiment I). In

563   Experiment II, a single hotspot was limited to the M1 region as well, and the deflection in S1

564   disappeared. The M1 hotspot was also slightly shifted inferior. The third subject belongs to the

565   group which showed a hotspot only in S1 in Experiment I. In Experiment II, however, the

566   hotspot moved to M1 supporting our assumption of insufficient information content concerning

567   the combination of electric field profiles and measured MEP amplitude curves due to a limited

568   classification ability of the electric fields. As indicated by the convergence results of the

569   permutation study (Fig. 8a), adding the remaining conditions of Experiment II (20-of-20 case)

570   does not yield any improvement for any of the three subject groups.

571   For subject S1 (first row in Fig. 9), the cross-correlation of the electric field distributions in the

572   ROI was 0.951 for Experiment I, and 0.921 for Experiment II. For subject S8 (second row in

573   Fig. 9), the cross-correlation was 0.953 and 0.925 for Experiment I and II, respectively. We

574   observed that the use of less correlating electric field distributions increased the quality of the

575   reconstruction. Finally, for subject S12 (third row in Fig. 9) the cross-correlations were nearly

576   the same with 0.951 and 0.953 from Experiment I to II, respectively. However, the

577   improvement of the results indicates that the selected coil positions and orientations in

578   Experiment II were more suitable to determine the congruence factor, resulting in a higher

579   distinguishability between the cortical positions in Experiment I. We wish to emphasize that

580   this property is only partly reflected by the cross-correlation coefficient. A definition of a more

581   sophisticated ambiguity measure to determine an optimal set of coil positions and orientations
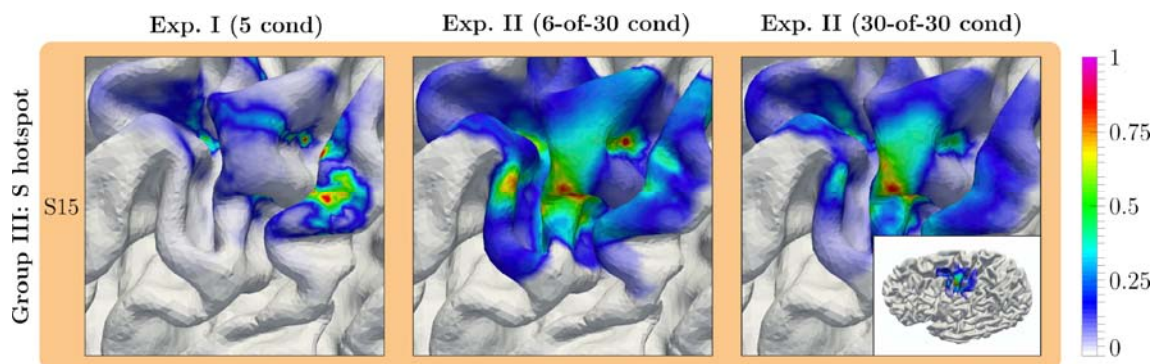
582   will be subject of a future study.
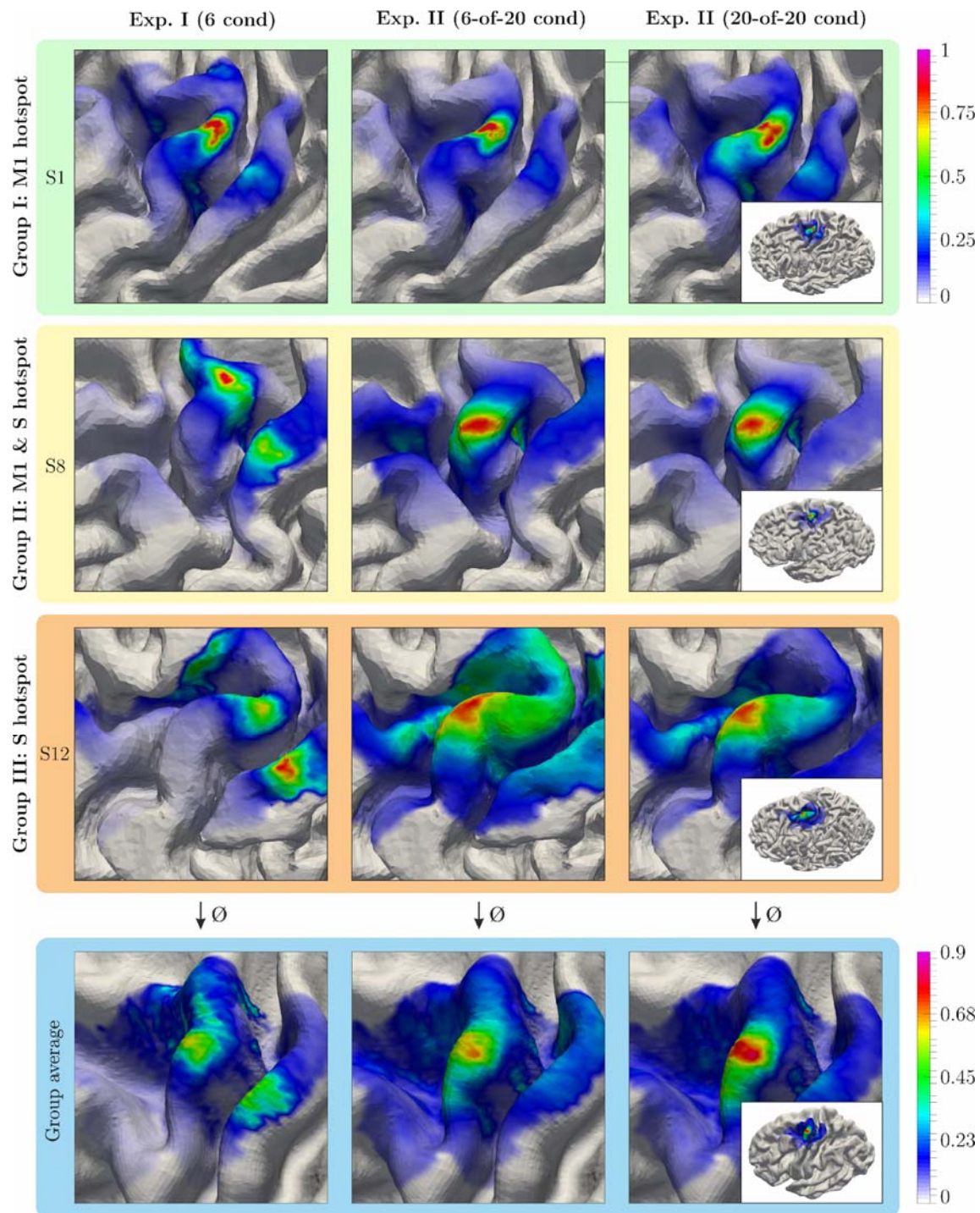
Figure 9. Normalized congruence factor maps of 3 subjects. The first column shows the results of Experiment I with 6 experimental conditions; the middle row depicts the 6-of-20 condition combination with the smallest hotspot area from Experiment II; The right column shows the congruence factor maps when all 20 experimental conditions of study II are included in the analysis. The subjects were chosen to include on participant from each result group in study I (M1 only, M1 and S1, S1 only, see Fig.7).

589 **3.3 Validation**

590 After determining the optimal coil positions and orientations for the subjects in Experiment II,

591 we validated the predicted cortical sites of stimulation. For health reasons not related to this

592 study, subject 12 from group III (c.f. Fig. 9) was not able to participate in the validation study.

593 We replaced that subject by subject 15 from group III and repeated Experiment II. It turned

594 out that, in this subject, using the predefined 20 conditions did not yield a single pronounced

595 congruence factor hotspot. To increase the electric field variance, we added further conditions

596 at different positions, orientations, and tilting angles of the TMS coil (see Fig. S5 of

597 *Supplemental Material*). We additionally determined the corresponding best 6-of-30 condition

598 combination yielding very similar results compared to the result to the full 30 condition

599 analysis. The results are shown in Fig. 10.

600 We measured the lowest MTs at these optimal coil positions and orientations compared to all

601 other tested coil configurations (Fig. 11). Notably, all computationally determined optimal coil

602 orientations are fairly similar to the commonly used 45° coil orientation towards the *fissura*

603 *longitudinalis* (Brasil-Neto et al., 1992; Mills et al., 1992).

604

605 **Figure 10.** Normalized congruence factor maps of subject 15, replacing subject 12 from subject group III for
606 the validation. The first column shows the results of Experiment I with 5 experimental conditions; the
607 middle row depicts the 6-of-30 condition combination with the smallest hotspot area from Experiment II;
608 the right column shows the congruence factor map when all 30 experimental conditions of study II are
609 taken into account.

28
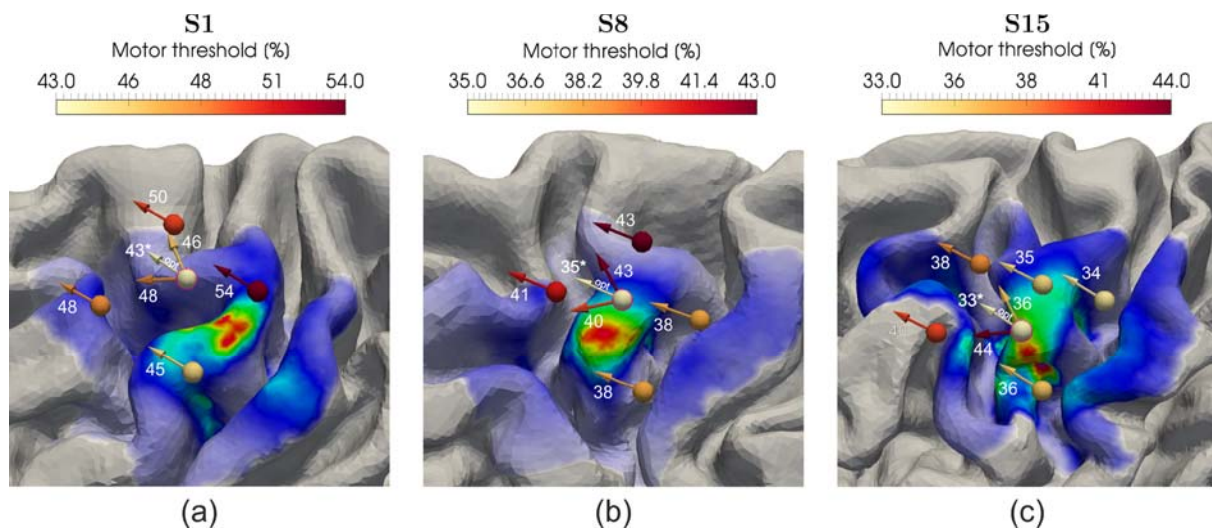
Figure 11. Coil positions and orientations used to validate the determined cortical site of stimulation. The optimal coil position is marked with a dashed purple circle and its corresponding optimal orientation is indicated by "opt". Numbers represent the resting motor thresholds determined where 5 of 10 consecutive MEPs reached values > 50 µV. Lowest MTs at the optimal coil positions and orientations are marked with an asterisk.
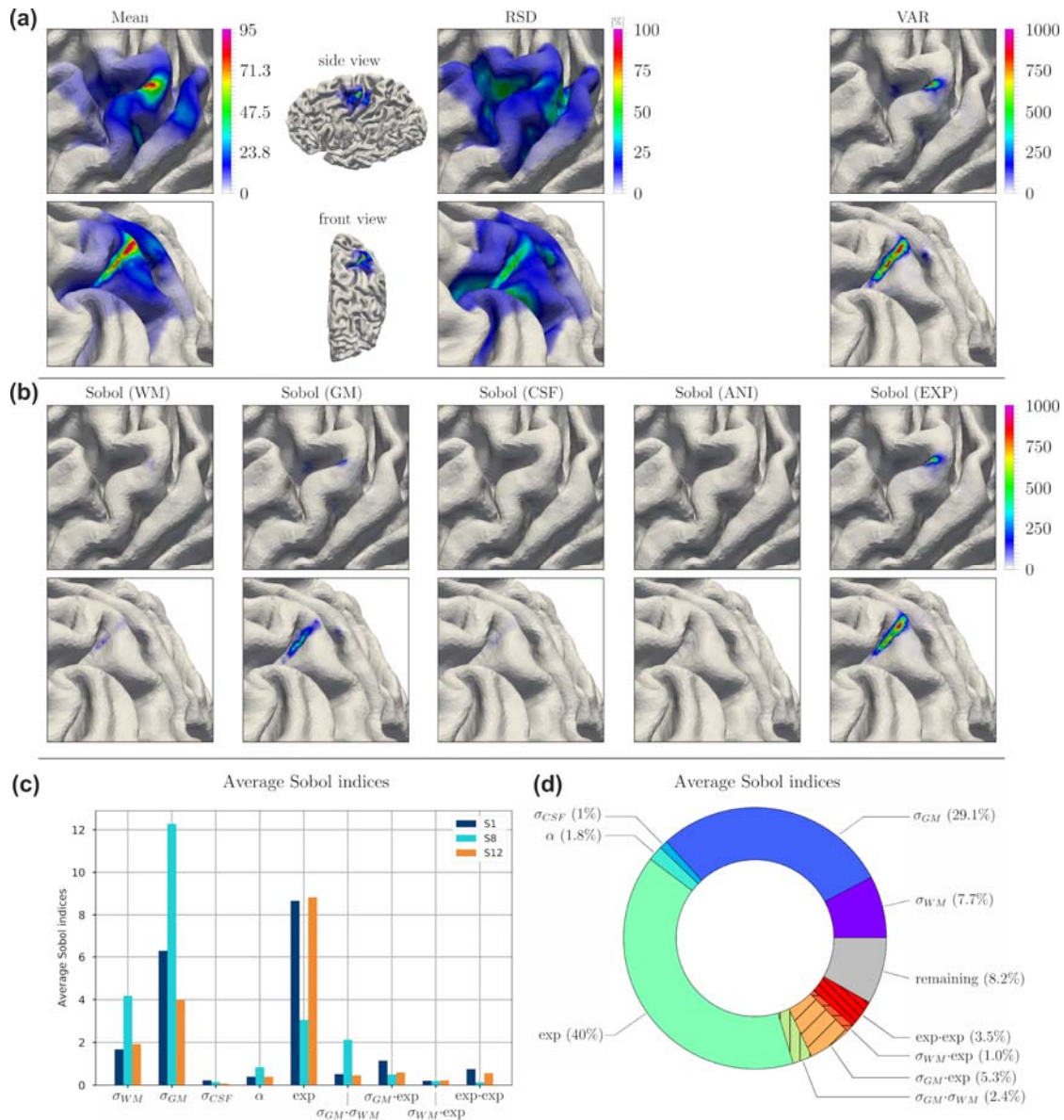
3.4 Uncertainty and sensitivity analysis

We analyzed the congruence factor results in terms of uncertainties and sensitivities towards the electrical conductivities of brain tissues, fractional anisotropy, and measurement inaccuracies for all subjects of Experiment II considering the 6-of-20 case described previously. The results from subject S1 are shown in Fig. 11. The results of subject S8 and S12 are shown in Fig. S8 and Fig. S9. The uncertainties of the model parameters are listed in Table 1 and Table S1 & S2. The spatial distributions of the mean, the relative standard deviation (RSD), and the variance (VAR) of the congruence factor are shown in Fig. 12a. The mean distribution shows a hotspot, which is extending from the gyral crown of M1 to upper parts of the anterior sulcal wall. RSD and VAR indicate that, the congruence factor could be determined with a greater certainty ($RSD \approx 12\%$) on the gyral crown than on the anterior sulcal wall ($RSD \approx 40\%$).

To identify the most influential model parameters, we decomposed VAR into its origins by a Sobol decomposition. The spatial distributions of the absolute first order Sobol indices on the cortex are shown in Fig. 12b. The Sobol coefficient maps of the MEP curve parameters are accumulated to one Sobol index termed Sobol (EXP). The average first and highest second

632   order Sobol indices are depicted in Fig. 12c for all subjects of Experiment II. The average was

633   computed over the elements in the ROI. The most protrude parameters that contribute to the

634   uncertainty of the congruence factor were the electrical conductivities of GM (σ_{GM}), WM (σ_{WM})

635   as well as the uncertainty of the measured MEP curves (EXP) for all subjects. Their relative

636   contribution to the total variance, shown in Fig. 12 d (and in Fig. S8d and S9d), was subject

637   specific and depended on the accuracy of the measured MEP curves as well as the brain

638   anatomy, influencing the electric field distribution. The uncertainty of the congruence factor

639   hotspot in the anterior sulcal wall predominantly originated from the uncertainty of σ_{GM} and the

640   measurement uncertainties indicate that this hotspot is likely to be spurious.

641

642

643

Figure 12: Uncertainty and sensitivity analysis of the congruence factor determined for subject S1 in the 6-of-20 analysis of Experiment II. (a) Expected value (Mean), relative standard deviation (RSD), and variance (VAR) of the congruence factor. (b) Spatial distributions of the absolute first order Sobol indices. The normalization with respect to the total variance was avoided to strengthen the focus on regions of high variance (see eq. (12) in the *Supplementary Material* on how the Sobol indices are computed). The Sobol index maps of the individual MEP parameters resulting from uncertainties in the experimental data are summarized into one Sobol index map "Sobol (EXP)". (c) Average first order Sobol indices for subjects S1 (shown here), S8, and S12. The average was computed over the elements in the ROI (d) Relative first order Sobol indices averaged over the ROI. For (a) and (b) two different perspectives are shown (top and bottoms rows), in order to improve visibility of the effects.

31

653 **4 DISCUSSION**

654 **4.1 Summary of Findings**

655 In the present study, we introduce a novel approach that links numerical modeling of the

656 induced electric field with measurements of peripheral physiological responses to considerably

657 improve the localization of effectively stimulated areas during TMS. With this approach, we

658 were able to accurately localize the cortical area that is responsible for the observed motor

659 output when single TMS pulses were applied over the motor cortex. Our main finding was that

660 sharply bounded neural structures located in the gyral crowns extending to the upper parts of

661 the sulcal wall of the motor hand area represent the most likely origin of the motor evoked

662 potentials. We identified the magnitude and the tangential component of the electric field as

663 the relevant quantities for modulating the observed effect.

664 Our results implicate that unique results can be obtained with relatively few measurements.

665 Based on our findings, we derive principles for the selection of the respective coil positions that

666 may help to improve localization of TMS effects in future applications, both at the single

667 subject and group level. Our first experiment combined two different stimulation sites with

668 three coil rotations each, yielding 6 conditions. The induced electric fields were computed with

669 FEM, allowing for the assessment of element-wise E-MEP relations. We identified three groups

670 with a hotspot at either M1, the somatosensory cortex, or both. One subject from each group

671 was included in the extended second experiment. For the subject from the M1-group, the

672 hotspot was replicated at the same spot. For the subjects from the other two groups, the

673 results could be significantly improved and single hotspots at the gyral crowns and the upper

674 parts of the sulcal walls of the motor hand area were observed in all cases. The final validation

675 study in three subjects confirmed that optimizing the TMS coil position and orientation such

676 that it maximized the electric field at the predicted cortical target indeed resulted in a

677 minimization of the MTs.

678 The congruence factor employed in our study quantifies the correlation between the measured

679 physiological variable (here, the MEP) and the induced electric field profiles. Note that the

680 proposed approach does not depend on the involved function types to describe the I/O

681 behavior. This provides a high level of flexibility and makes the method easy to adapt to other

682   applications and domains. We conclude that our approach significantly improves the

683   localization of effectively stimulated areas during TMS and may increase the power and

684   reliability of the resulting effects in future TMS studies at the individual level.

685   **4.2 Relation to prior studies relating TMS electric fields with MEPs**

686   Based on our results, we argue that areas with maximum congruence factors are good

687   candidates for effective stimulation. Importantly, in all subjects, we observed that higher

688   variability between electric fields sharpened the localization results. Sets of experimental

689   conditions that selectively varied coil position or coil orientation did not contain sufficient

690   information to uniquely determine the effective cortical stimulation site. Moreover, stimulation

691   directly over M1 with 45° orientation, though yielding the strongest effect, was by far not the

692   most informative condition in our method, which can be explained by the relative wide spread

693   of the electric field in the motor area, and hence, with low discriminative power, produced by

694   standard figure-of-eight coils. These observations might provide a potential explanation for the

695   spurious second hotspot in the somatosensory cortex observed by Bungert et al. (2017) when

696   stimulating selectively over M1 and Laakso et al. (2018), stimulating with a 45° coil orientation

697   towards the *fissura longitudinalis* (Brasil-Neto et al., 1992; Mills et al., 1992). Notably, we

698   observed similar effects in Experiment I, where only 5 or 6 non-optimal experimental

699   conditions were considered (subject group II and III, Fig. 7). Reducing the correlation of the

700   electric fields across the tested positions and orientations considerably enhanced the

701   localization capabilities of our method in all subjects (Experiment II). This observation was

702   further supported by a permutation analysis showing that higher variability between the spatial

703   patterns of the electric fields, by means of using particular combinations of coil positions and

704   orientations, considerably increased the accuracy of the localization results.

705   Interestingly, studies incorporating selectively the 45° coil orientation towards the *fissura*

706   *longitudinalis* (Laakso et al., 2018; Krieg et al., 2013; Salinas et al., 2011) appear to support

707   sulcal wall activation by the normal component of the electric field. In contrast, studies which

708   involve different coil orientations (Bungert et al., 2017) highlight $|E|$ and gyral crowns. Recent

709   results from direct electric stimulation (Aonuma et al., 2018) support the notion of gyral crown

710   activation, which contrasts with the conclusions drawn from applying imaging techniques (Fox

711 et al., 2004; Krieg et al., 2013). However, both methods have the major disadvantage that

712 their resolution in the current state of research is not sufficient to answer this question. By

713 changing both, i.e. coil position and orientation, we observed low congruence factors for the

714 normal component of the electric field at the anterior wall of the central sulcus. Since low

715 congruence factors highlight areas where the behavioral effect does *not* correlate with changes

716 in the local electric field, our results indicate that the previously proposed stimulation

717 mechanism by the normal component (Laakso et al., 2018; Fox et al., 2004; Krieg et al.,

718 2013) cannot explain the observed effect for all experimental conditions. In contrast, we found

719 that the tangential component (and therefore also the magnitude) of the field showed

720 reasonable congruence factor maps. This finding suggests that the gyral crowns and upper

721 parts of the sulcal wall are the most likely origin of the motor evoked potentials.

722 Two prior studies superimposed the calculated electric fields either in additive or multiplicative

723 fashion to localize the cortical position targeted by TMS (Opitz et al., 2013; Aonuma et al.,

724 2018). Opitz et al. (2013) weighted the computed electric fields with the strengths of the

725 observed effects and overlaid the fields in an additive fashion. In contrast, Aonuma et al.

726 (2018) superimposed the fields in a multiplicative fashion after selecting the experimental

727 conditions for which the observable effect exceeded a particular threshold. The latter may be

728 disadvantageous since it uses only a small portion of the information contained in the

729 measurement. Both methods approximate a covariance between the field strength and the

730 MEP amplitude. However, this covariance does not only depend on the correlative relationship

731 between the two, but also on the general magnitude of the field across conditions. This leads

732 to a strong bias towards voxels which generally receive higher field strengths (i.e., on gyral

733 crowns) for both approaches.

734 Our validation study confirmed the general optimality of the PA-45 coil orientation towards the

735 *fissura longitudinalis* (Brasil-Neto et al., 1992; Mills et al., 1992). The slight deviations

736 between the optima confirm the inter-individual variability in optimal coil orientation observed

737 for example by Balslev et al. (2007) and Bungert et al. (2017).

738 **4.3 Relation to simulations of neural excitation by TMS**

739 Combining electric field computations and compartment models of neurons, Seo et al. (2017)

740 propose the initial segments of pyramidal cells in layer 3 and 5 to be the sites of effective

741 stimulation, possibly due to the omnidirectional orientation of the basal dendritic trees.

742 Alternatively, also the terminals of axon collaterals might be stimulated (Aberra et al., 2018),

743 which again are equally distributed in all directions around the main axon and have low

744 thresholds. Our results, namely high congruence factors of the magnitude and the tangential

745 component of the electric field in the gyral crown and rim, indicate that the stimulation

746 mechanism of TMS may indeed occur due to synaptic or dendritic activation of neurons. This is

747 in line with predictions from previous modeling studies (Silva et al., 2008; Salvador et al.,

748 2011). Future studies may extend the congruence factor approach to more detailed neuron

749 models (Moezzi et al., 2018) and tractography-based fiber tracts (De Geeter et al., 2015; De

750 Geeter et al., 2016).

751 **4.4 Factors influencing the stability of the results**

752 The uncertainty and sensitivity analyses confirmed robust hotspots on the gyral crowns

753 extending to upper parts of the sulcal wall of M1 (cf. Fig. 10, Fig. S8, and Fig. S9). The

754 maxima of the means coincide well with the results of the deterministic case (cf. Fig. 9). The

755 relative standard deviation (RSD) in the hotspots on the gyral crowns varies between 10-25%,

756 depending on the subject. The uncertainties mainly translate into uncertainties of the

757 congruence factor on the anterior sulcal wall of the precentral gyrus and not on the gyral

758 crown, where the primary hotspot was detected.

759 The hotspots on the anterior sulcal wall are lying in line with the normal vector from the head

760 surface towards the center of the brain. We hypothesize that these spurious hotspots are

761 projections from the gyral crown hotspots. Since our approach is independent of the

762 magnitudes of the electric field, but sensitive to their spatial profiles, these spurious hotspots

763 might result from insufficient electric field variance between these locations.

764 Decomposing the variance into their origins revealed a strong contribution from GM and WM

765 conductivity as well as from the measured I/O curves. This is in line with previous studies,

766 which showed that the electrical conductivities of GM and WM are the most influencing

767 parameters considering the induced electric field in grey matter (Weise et al., 2015; Codecasa

768 et al., 2016; Saturnino et al., 2018). The impact of the measurement uncertainty was lower

769   for subject S8 compared to the other subjects, which can be explained by the fact that the MEP

770   curves could be determined with a higher certainty (cf. Table 1, S1, and S2). Nevertheless, its

771   contribution was still high and special care should be taken when recording characteristic

772   regions of the I/O curve, like the turning points of the sigmoids, to reduce its influence on the

773   congruence factor. In contrast, the conductivity of CSF and the level of anisotropy had a small

774   impact on the congruence factor and could be treated as deterministic in future analyses.

4.5 Towards a clinically suitable, principled TMS mapping procedure

775

776   To enable clinical applicability of the proposed method, for instance in presurgical mapping, the

777   experimental effort has to be reduced to a minimum while ensuring reliability. Regarding our

778   second research question, the permutation analysis from Experiment II (Fig. 8, Fig. S6, and

779   Fig. S7) revealed that six stimulation conditions at three different locations around M1 with

780   different orientations are sufficient to address the localization problem at hand. Notably, the

781   actual condition combinations that result in a minimum hotspot area differ strongly between

782   subjects. This is likely due to inter-individual differences in anatomy and functional brain

783   organization. Using a high number of experiments increases the stability and reliability of the

784   solution. However, at the same time, it also reduces the resolution by introducing more

785   measurement uncertainty. This became evident in the permutation study in Fig. 8b, where the

786   minimal hotspot area had a minimum for $k = 6$ conditions and slightly increased for higher

787   values of k. Increasing the field variability is a promising starting point for subject specific

788   optimization to determine the optimal number and selection of coil positions and orientations

789   before the experiment. An even more sophisticated scheme could involve maximizing the

790   distinguishability between voxels based on their sensitivity profiles, that is, the vectors of E

791   fields caused by the different coil positions and orientations with identical activation strength.

792   In order to distinguish two voxels with respect to their congruence factor, their sensitivity

793   profiles should be as different as possible. The formulation of an optimization procedure that

794   identifies the best combination of coil positions and orientations to maximize the differences of

795   the sensitivity profiles between any two voxels in the region of interest will be investigated in

796   detail in future research.

797   Beyond the localization of the origin of MEPs, our approach allows to localize functionally

798   involved cortical areas for other processes, provided that it is possible to observe a

799   quantitative response variable that depends on the stimulation intensity. Considering adapted

800   experimental paradigms, which are able to capture this, future studies may use our approach

801   for pre-surgical language or somatosensory mapping purposes.

802   **4.6 Study Limitations**

803   Our results indicate that possible carry-over effects of stimulation in Experiment II due to the

804   relatively short inter stimulus interval (ISI) of 4 s do not affect our conclusions, as the ISI was

805   kept stable during a single experiment and any carry-over effect should be stable as well.

806   Therefore, the correlative relationship between electric field and MEP amplitude should remain

807   unaffected, even if the absolute value of the MEP is changed.

808   So far, our method relies on the assumption that the experimental effects can be explained by

809   activity in a single cortical patch. This holds in the current motor experiment identifying the

810   cortical origin of FDI activation. In other experimental paradigms, however, several network

811   nodes may exist that might influence the effect. These nodes may also influence each other in

812   different ways, which would lead to partial correlations. Incorporating connections into our

813   model will tremendously increase the computational cost and efficient algorithms have to be

814   developed to combine the electric field profiles and the physiological response data. Since

815   numerous connections can be analyzed independently from each other, the problem is highly

816   parallelizable and well suited for GPU or HPC implementations. The extension of our technique

817   to identify multivariate relationships between externally observable effects and stimulation of

818   neural populations is subject of ongoing work.

Acknowledgments

References

Aberra, AS, Peterchev AV, Grill WM. Biophysically realistic neuron models for simulation of cortical stimulation. J. Neural Eng. 2018; 15(6):66023. (doi: 10.1088/1741-2552/aadbb1)

Akaike, H. A new look at the statistical model identification. IEEE Trans. Automat. Contr. 1974; 19(6):716-723. (doi: 10.1109/TAC.1974.1100705)

Akhtari M, Mandelkern M, Bui D, Salamon N, Vinters HV, Mathern GW. Variable anisotropic brain electrical conductivities in epileptogenic foci. Brain Topogr 2010; 23(3):292-300. (doi: 10.1007/s10548-010-0144-z)

Aonuma S, Gomez-Tames J, Laakso I, Hirata A, Takakura T, Tamura M, Muragaki Y. A high-resolution computational localization method for transcranial magnetic stimulation mapping. NeuroImage 2018; 172(1):85–93. (doi: 10.1016/j.neuroimage.2018.01.039)

Askey R, Wilson JW. Some Basic Hypergeometric Orthogonal Polynomials that Generalize Jacobi-Polynomials. Mem Amer Math Soc 1985; 54(319):1–55. (ISBN: 9780821860557)

Balslev D, Braet W, McAllister C, Miall RC. Inter-individual variability in optimal current direction for transcranial magnetic stimulation of the motor cortex. Journal of neuroscience methods 2007, 162(1-2): 309-313. (doi: 10.1016/j.jneumeth.2007.01.021)

Baumann SB, Wozny DR, Kelly SK, Meno FM. The Electrical Conductivity of Human Cerebrospinal Fluid at Body Temperature. IEEE Trans Biomed Eng 1997; 44(3):220-223. (doi: 10.1109/10.554770)

Bestmann S. The physiological basis of transcranial magnetic stimulation. Trends Cogn Sci 2008; 12: 81-83. (doi: 10.1016/j.tics.2007.12.002)

Bestmann S. Computational neurostimulation in basic and translational research. Prog Brain Res 2015; 222: xv-xx. (doi: 10.1016/S0079-6123(15)00159-4)

Bestmann S, Feredoes E. Combined neurostimulation and neuroimaging in cognitive neuroscience: past, present, and future. Ann N Y Acad Sci 2013; 1296: 11-30. (doi: 10.1111/nyas.12110)

Bikson M, Truong DQ, Mourdoukoutas AP, Aboseria M, Khadka N, Adair D, Rahman A. Modeling sequence and quasi-uniform assumption in computational neurostimulation. Prog Brain Res 2015; 222: 1-23. (doi: 10.1016/bs.pbr.2015.08.005)

857 Brasil-Neto JP, Cohen LG, Panizza M, Nilsson J, Roth BJ, Hallett, M (1992). Optimal focal
858 transcranial magnetic activation of the human motor cortex: effects of coil orientation, shape
859 of the induced current pulse, and stimulus intensity. Journal of clinical neurophysiology 9(1),
860 132-136. (PMID: 1552001)

861 Bungert A, Antunes A, Espenhahn S, Thielscher A. Where does TMS Stimulate the Motor
862 Cortex? Combining Electrophysiological Measurements and Realistic Field Estimates to Reveal
863 the Affected Cortex Position. Cereb Cortex 2017; 27: 5083-5094. (doi:
864 10.1093/cercor/bhw292)

865 Codecasa L, Di Rienzo L, Weise K, Gross S, Haueisen J. Fast MOR-based Approach to
866 Uncertainty Quantification in Transcranial Magnetic Stimulation. IEEE Trans Magn 2016;
867 52(3):7200904. (doi: 10.1109/TMAG.2015.2475120)

868 Conforto AB, Z'Graggen WJ, Kohl AS, Rösler KM, Kaelin-Lang A. Impact of coil position and
869 electrophysiological monitoring on determination of motor thresholds to transcranial magnetic
870 stimulation. Clin Neurophysiol 2004; 115(4): 812-819. (doi: 10.1016/j.clinph.2003.11.010)

871 Datta A, Bikson M, Fregni F. Transcranial direct current stimulation in patients with skull
872 defects and skull plates: high-resolution computational FEM study of factors altering cortical
873 current flow. Neuroimage 2010; 52: 1268-1278. (doi: 10.1016/j.neuroimage.2010.04.252)

874 Dale AM, Fischl B, Sereno MI. Cortical surface-based analysis. I. Segmentation and surface
875 reconstruction. NeuroImage 1999; 9(2): 179-194. (doi: 10.1006/nimg.1998.0395)

876 De Geeter N, Crevecoeur G, Leemans A, Dupré L. Effective electric fields along realistic DTI-
877 based neural trajectories for modelling the stimulation mechanisms of TMS. Physics in
878 medicine and biology 2015; 60(2): 453-471. (doi: 10.1088/0031-9155/60/2/453)

879 De Geeter N, Dupré L, Crevecoeur G. Modeling transcranial magnetic stimulation from the
880 induced electric fields to the membrane potentials along tractography-based white matter fiber
881 tracts. J. Neural Eng. 2016a; 13(2):26028. (doi: 10.1088/1741-2560/13/2/026028)

882 De Geeter, N, Lioumis, P, Laakso A, Crevecoeur G, Dupre L. How to include the variability of
883 TMS responses in simulations: a speech mapping case study. Physics in medicine and biology
884 2016b; 61(21): 7571-7585. (doi: 10.1088/0031-9155/61/21/7571)

885 De Lucia M, Parker GJ, Embleton K, Newton JM, Walsh V. Diffusion tensor MRI-based
886 estimation of the influence of brain tissue anisotropy on the effects of transcranial magnetic
887 stimulation. Neuroimage 2007; 36: 1159-1170. (doi: 10.1016/j.neuroimage.2007.03.062)

888 Di Lazzaro V, Profice P, Ranieri F, Capone F, Dileone M, Oliviero A, Pilato F (2012). I-wave
889 origin and modulation. Brain Stimulation 5(4). (doi: 10.1016/j.brs.2011.07.008)

890 Di Lazzaro V, Rothwell JC (2014). Corticospinal activity evoked and modulated by non-invasive
891 stimulation of the intact human motor cortex. J Physiol 592(19). (doi:
892 10.1113/jphysiol.2014.274316)

893 Fischl B, Sereno MI, Dale AM. Cortical surface-based analysis. II: Inflation, flattening, and a
894 surface-based coordinate system. NeuroImage 1999; 9(2): 195-207. (doi:
895 10.1006/nimg.1998.0396)

896 Fox PT, Narayana S, Tandon N, Sandoval H, Fox SP, Kochunov P, Lancaster JL. Column-based
897 model of electric field excitation of cerebral cortex. Hum Brain Mapp 2004; 22: 1-14. (doi:
898 10.1002/hbm.20006)

899 Gabriel C, Peyman A, Grant EH. Electrical conductivity of tissue at frequencies below 1 MHz.
900 Phys Med Biol 2009; 54(16):4863-4878. (doi: 10.1088/0031-9155/54/16/002)

901 Ghanem R, Higdon D, Owhadi H. Handbook of Uncertainty Quantification. Cham: Springer;
902 2016. (doi: 10.1007/978-3-319-12385-1)

903 Güllmar D, Haueisen, J, Reichenbach, JR. Influence of anisotropic electrical conductivity in
904 white matter tissue on the EEG/MEG forward and inverse solution. A high-resolution whole
905 head simulation study. NeuroImage 2010; 51(1): 145-163. (doi:
906 10.1016/j.neuroimage.2010.02.014)

907 Hallett M. Transcranial magnetic stimulation and the human brain. Nature 2000; 406: 147-
908 150. (doi: 10.1038/35018000)

909 Hamada M, Murase N, Hasan A, Balaratnam M, Rothwell JC. The role of interneuron networks
910 in driving human motor cortical plasticity. Cereb Cortex 2013; 23: 1593-1605. (doi:
911 10.1093/cercor/bhs147)

912 Hartwigsen G, Bergmann TO, Herz DM, Angstmann S, Karabanov A, Raffin E, Thielscher A,
913 Siebner HR (2015). Modeling the effects of noninvasive transcranial brain stimulation at the
914 biophysical, network, and cognitive Level. Prog Brain Res; 222: 261-287. (doi:
915 10.1016/bs.pbr.2015.06.014)

916 Jenkinson M, Beckmann CF, Behrens TE, Woolrich MW, Smith SM. FSL. NeuroImage 2012;
917 62(2): 782-790. (doi: 10.1016/j.neuroimage.2011.09.015)

918 Krieg TD, Salinas FS, Narayana S, Fox PT, Mogul DJ. PET-based confirmation of orientation
919 sensitivity of TMS-induced cortical activation in humans. Brain Stimulation 2013; 6(6):898-
920 904. (doi: 10.1016/j.brs.2013.05.007)

921 Krieg, S, Tarapore PE, Picht T, Tanigawa N, Houde J, Sollmann N, Meyer B, Vajkoczy P, Berger
922 SB, Ringel F, Nagarajan S. Optimal timing of pulse onset for language mapping with navigated
923 repetitive transcranial magnetic stimulation. NeuroImage 2014; 100, 219–236. (doi:
924 10.1016/j.neuroimage.2014.06.016)

925 Laakso I, Murakami T, Hirata A, Ugawa Y. Where and what TMS activates: Experiments and
926 modeling. Brain Stimul 2018; 11: 166-174. (doi: 10.1016/j.brs.2017.09.011)

927 Le Maitre OP, Knio OM. Spectral Methods for Uncertainty Quantification. Dordrecht: Springer,
928 2010. (doi: 10.1007/978-90-481-3520-2)

929 Li C, Bak AF, Parker LO. Specific resistivity of the cerebral cortex and white matter. Exp Neurol
930 1968; 20(4):544-557. (doi: 10.1016/0014-4886(68)90108-8)

931 Logothetis NK, Kayser C, Oeltermann A. In vivo measurement of cortical impedance spectrum
932 in monkeys: implications for signal propagation. Neuron 2007; 55(5):809-823. (doi:
933 10.1016/j.neuron.2007.07.027)

934 Mayka MA, Corcos DM, Leurgans SE, Vaillancourta DE. Three-dimensional locations and
935 boundaries of motor and premotor cortices as defined by functional brain imaging. A meta-
936 analysis. Neuroimage 2006; 31(4): 1453–1474. (doi: 10.1016/j.neuroimage.2006.02.004)

937 Mills KR, Boniface SJ, Schubert M. Magnetic brain stimulation with a double coil: the
938 importance of coil orientation. Electroencephalography and Clinical Neurophysiology/Evoked
939 Potentials 1992, 85(1): 17-21. (doi: 10.1016/0168-5597(92)90096-T)

940 Miniussi C, Harris JA, Ruzzoli M. Modelling non-invasive brain stimulation in cognitive
941 neuroscience. Neurosci Biobehav Rev 2013; 37: 1702-1712. (doi:
942 10.1016/j.neubiorev.2013.06.014)

943 Moezzi, B Schaworonkow N, Plogmacher L, Goldsworthy MR, Hordacre B, Mcdonnell M, Iannella
944 N, Ridding MC, Triesch, J (2018). Simulation of electromyographic recordings following
945 transcranial magnetic stimulation. Journal of neurophysiology. (doi: 10.1152/jn.00626.2017)

946 Neggers SF, Petrov PI, Mandija S, Sommer IE, van den Berg NA. Understanding the
947 biophysical effects of transcranial magnetic stimulation on brain tissue: the bridge between
948 brain stimulation and cognition. Prog Brain Res 2015; 222: 229-259. (doi:
949 10.1016/bs.pbr.2015.06.015)

950   Nicholson PW. Specific impedance of cerebral white matter. Exp Neurol 1965; 13(4):386-401.
951   (doi: 10.1016/0014-4886(65)90126-3)

952   Oldfield, R.C., 1971. The assessment and analysis of handedness: The Edinburgh inventory.
953   Neuropsychologia 9, 97–113. (doi:10.1016/0028-3932(71)90067-4)

954   Opitz A, Legon W, Rowlands A, Bickel WK, Paulus W, Tyler WJ. Physiological observations
955   validate finite element models for estimating subject-specific electric field distributions induced
956   by transcranial magnetic stimulation of the human motor cortex. Neuroimage 2013; 81: 253-
957   264. (doi: 10.1016/j.neuroimage.2013.04.067)

958   Opitz A, Windhoff M, Heidemann RM, Turner R, Thielscher A. How the brain tissue shapes the
959   electric field induced by transcranial magnetic stimulation. Neuroimage 2011; 58: 849-859.
960   (doi: 10.1016/j.neuroimage.2011.06.069)

961   Opitz, A., Legon, W., Rowlands, A., Bickel, W. K., Paulus, W., & Tyler, W. J. (2013).
962   Physiological observations validate finite element models for estimating subject-specific electric
963   field distributions induced by transcranial magnetic stimulation of the human motor cortex.
964   NeuroImage, 81, 253-264. (doi: 10.1016/j.neuroimage.2013.04.067)

965   Opitz A, Zafar N, Bockermann V, Rohde V, Paulus W. Validating computationally predicted TMS
966   stimulation areas using direct electrical stimulation in patients with brain tumors near
967   precentral regions. NeuroImage. Clinical 2014; 4: 500-507. (doi: 10.1016/j.nicl.2014.03.004)

968   Pascual-Leone A, Torres F. Plasticity of the sensorimotor cortex representation of the reading
969   finger in Braille readers. Brain 1993; 116(1): 39-52. (PMID: 8453464)

970   Penny W, Friston K, Ashburner J, Kiebel S, Nichols T. Statistical Parametric Mapping: The
971   Analysis of Functional Brain Images, Academic Press, 2007, 1st Edition (ISBN
972   9780123725608)

973   Picht, T. (2014). Current and potential utility of transcranial magnetic stimulation in the
974   diagnostics before brain tumor surgery. CNS oncology, 3(4), 299-310. (doi:
975   10.2217/cns.14.25)

976   Ranck JB. Specific impedance of rabbit cerebral cortex. Exp Neurol 1963; 7:144-152. (doi:
977   10.1016/S0014-4886(63)80005-9)

978   Rossi, S., Hallett, M., Rossini, P.M., Pascual-Leone, A., 2009. Safety, ethical considerations,
979   and application guidelines for the use of transcranial magnetic stimulation in clinical practice
980   and research. Clin. Neurophysiol. 120, 2008–39. (doi:10.1016/j.clinph.2009.08.016)

981   Rothwell JC, Hallett M, Berardelli A, Eisen A, Rossini P, Paulus W (1999). Magnetic stimulation:
982   motor evoked potentials. Electroencephalogr Clin Neurophysiol Suppl, 52, 97-103. (PMID:
983   10590980)

984   Salinas FS, Szabó CÁ, Z W, Jones L, Leland MM, Wey HY, Duong TQ, Fox PT, Narayana S.
985   Functional neuroimaging of the baboon during concurrent image-guided transcranial magnetic
986   stimulation. NeuroImage 2011; 57(4):1393-1401. (doi: 10.1016/j.neuroimage.2011.05.065)

987   Salvador, R., Silva, S., Basser, P. J., & Miranda, P. C. (2011). Determining which mechanisms
988   lead to activation in the motor cortex: a modeling study of transcranial magnetic stimulation
989   using realistic stimulus waveforms and sulcal geometry. Clinical neurophysiology, 122(4), 748-
990   758. (doi 10.1016/j.clinph.2010.09.022)

991   Sandrini M, Umilta C, Rusconi E. The use of transcranial magnetic stimulation in cognitive
992   neuroscience: a new synthesis of methodological issues. Neurosci Biobehav Rev 2011; 35:
993   516-536. (doi: 10.1016/j.neubiorev.2010.06.005)

994   Saturnino, G., Thielscher, A., Madsen, K. H., Knösche, T. R., Weise, K. (2018). A principled
995   approach to conductivity uncertainty analysis in electric field calculations. NeuroImage. in
996   press. (doi: 10.1016/j.neuroimage.2018.12.053)

997 Seo H., Schaworonkow N., Jun S. C., Triesch J. (2017). A multi-scale computational model of
998 the effects of TMS on motor cortex. *F1000Research* 2017, **5**:1945 (doi:
999 10.12688/f1000research.9277.3)

1000 Siebner HR, Hartwigsen G, Kassuba T, Rothwell JC. How does transcranial magnetic
1001 stimulation modify neuronal activity in the brain? Implications for studies of cognition. Cortex
1002 2009; 45: 1035-1042. (doi: 10.1016/j.cortex.2009.02.007)

1003 Silva, S., Basser, P. J., & Miranda, P. C. (2008). Elucidating the mechanisms and loci of
1004 neuronal excitation by transcranial magnetic stimulation using a finite element model of a
1005 cortical sulcus. Clinical neurophysiology, 119(10), 2405-2413. (doi:
1006 10.1016/j.clinph.2008.07.248)

1007 Smith SM, Jenkinson M, Woolrich MW, Beckmann CF, Behrens TEJ, Johansen-Berg H, Bannister
1008 PR, De Luca M, Drobnjak I, Flitney DE, Niazy R, Saunders J, Vickers J, Zhang Y, De Stefano N,
1009 Brady JM, Matthews PM. Advances in functional and structural MR image analysis and
1010 implementation as FSL. NeuroImage 2004; 23(S1): 208-219. (doi:
1011 10.1016/j.neuroimage.2008.10.055)

1012 Sobol IM. Global sensitivity indices for nonlinear mathematical models and their Monte Carlo
1013 estimates. Math Comput Simulat 2001; 55(1-3):271-280. (doi: 10.1016/S0378-
1014 4754(00)00270-6)

1015 Sudret B. Global sensitivity analysis using polynomial chaos expansions. Reliab Eng Syst Safe
1016 2008; 93(7):964–979. (doi: 10.1016/j.ress.2007.04.002)

1017 Tarapore, PE, Findlay AM, Honma SM, Mizuiri, D, Houde JF, Berger MS, & Nagarajan, SS.
1018 Language mapping with navigated repetitive TMS: Proof of technique and validation.
1019 NeuroImage 2013; 82:260–272. (doi: 10.1016/j.neuroimage.2013.05.018)

1020 Thielscher A, Antunes A, Saturnino GB. Field modeling for transcranial magnetic stimulation: A
1021 useful tool to understand the physiological effects of TMS? Conf Proc IEEE Eng Med Biol Soc
1022 2015; 222-225. (doi: 10.1109/EMBC.2015.7318340)

1023 Thielscher A, Opitz A, Windhoff M. Impact of the gyral geometry on the electric field induced
1024 by transcranial magnetic stimulation. Neuroimage 2011; 54: 234-243. (doi:
1025 10.1016/j.neuroimage.2010.07.061)

1026 Tuch DS, Wedeen VJ, Dale AM, George JS, Belliveau JW. Conductivity tensor mapping of the
1027 human brain using diffusion tensor MRI. Proceedings of the National Academy of Sciences of
1028 the United States of America 2001; 98(20): 11697-11701. (doi: 10.1073/pnas.171473898)

1029 Wagner TA, Zahn M, Grodzinsky AJ, Pascual-Leone A. Three-dimensional head model
1030 simulation of transcranial magnetic stimulation. IEEE Trans Biomed Eng 2004; 51(9): 1586-
1031 1598. (doi: 10.1109/TBME.2004.827925)

1032 Weise K, Di Rienzo L, Brauer H, Haueisen J, Toepfer H. Uncertainty Analysis in Transcranial
1033 Magnetic Stimulation Using Non-intrusive Polynomial Chaos Expansion. IEEE Trans Magn 2015;
1034 51(7):5000408. (doi: 10.1109/TMAG.2015.2390593)

1035 Windhoff M, Opitz A, Thielscher A. Electric field calculations in brain stimulation based on finite
1036 elements: an optimized processing pipeline for the generation and usage of accurate individual
1037 head models. Hum Brain Mapp 2013; 34: 923-935. (doi: 10.1002/hbm.21479)

1038 Woolrich MW, Jbabdi S, Patenaude B, Chappell M, Makni S, Behrens T, Beckmann C, Jenkinson
1039 M, Smith SM. Bayesian analysis of neuroimaging data in FSL. NeuroImage 2009; 45(S1): 173-
1040 86. (doi: 10.1016/j.neuroimage.2008.10.055)

1041 Yedlin M, Kwan H, Murphy JT, Nguyen-Huu H, Wong YC. Electrical conductivity in cat cerebellar
1042 cortex. Exp Neurol 1974; 43(3):555-569. (doi: 10.1016/0014-4886(74)90195-2)